The Thesis Committe for Juergen Herbert Walther
Certifies that this is the approved version of the following thesis:

Imaging molecular motor regulation at the single molecule level

APPROVED BY

SUPERVISING COMMITTEE:

George T. Shubeita, Supervisor

Ernst-Ludwig Florin

Imaging molecular motor regulation at the single molecule level

by

Juergen Herbert Walther

THESIS

Presented to the Faculty of the Graduate School of

The University of Texas at Austin

in Partial Fulfillment

of the Requirements

for the Degree of

Master of Arts

THE UNIVERSITY OF TEXAS AT AUSTIN

December 2013

Acknowledgments

I like to thank George, Rafael, Guil, Jake and everybody else in the lab, CNLD and the physics department for their support during my stay in Austin.

Imaging molecular motor regulation at the single molecule level

Juergen Herbert Walther, M.A.
The University of Texas at Austin, 2013

Supervisor: George T. Shubeita

Molecular motor proteins are responsible for the long range transport of vesicles and organelles inside living cells. A small number of motor types transport thousands of distinct cargoes to various regions in the cell at the same time. This requires that intracellular transport be tightly regulated, yet the details of how motor regulators and cofactors tune motor function remain unknown in most cases. *In-vitro* studies at the single motor level have been instrumental in understanding the function of individual motors. In this thesis work I developed the methodology to extend *in-vitro* experiments to interrogate motor regulation at the single molecule level. I describe my modifications to the microscope setup as well as the acquisition cycle that made this possible. By combining differential interference contrast microscopy with single molecule fluorescence imaging and optical trapping I was able to manipulate and image the cargo while imaging a fluorescently-labeled regulator binding at the site of the motors. I used lipid droplets purified from *Drosophila* embryos as cargoes. Lipid droplets are carried by the opposite polarity microtubule motors kinesin and dynein in the embryos, and bind

specifically to microtubules *in-vitro*. In the presence of ATP they exhibit long-range and short-range motility. For this proof-of-principle experiment I used fluorescently labeled AMPPNP, a non-hydrolysable analogue of ATP which binds to the motor domain of kinesin when microtubule-bound, to image the binding of the nucleotide to the motor and demonstrate the activity of the motors. While a large fraction of microtubule-bound droplets co-localized with a fluorescent AMPPNP molecule, non-specific binding of the nucleotide to the microscope slide surface prevented confirming the specificity of the colocalization events. Nevertheless, these data demonstrate the ability of the methodology to capture, in real time, the process of a regulator binding the motor at the single molecule level.

Table of Contents

Chapter 1

Introduction to intracellular transport and its regulation

1.1 Active intracellular transport

In eucaryotic cells, different vital processes occur in various places. To maintain cellular functions, distinct constituents like vesicles or organelles move to the appropriate locations. This phenomenon, intracellular motion, was first observed in the late 18th century by Bonaventura Corti in the alga Chara [53].

However, the crowded and entangled cytoplasm renders diffusion of these particles due to thermal motion inefficient for most processes. In fact, in many cell types diffusion driven by thermal fluctuations would take longer than a lifetime of a human for cargoes to arrive at the appropriate location. Thus, active short- and long-scale transport have to maintain the cell functions. There are several distinct mechanisms for active long-scale transport including actin polimerization, cytoplasmic streaming and movement along cytoskeletal tracks [59]. Molecular motor driven transport of cargoes along cytoskeletal tracks is the best understood and most important among these mechanisms. Active transport by dozens of different kinds of motor proteins guarantees the shipment of the molecules to the right spots in the cell. As an analogy consider the cell as a city which has to organize the delivery of goods to specific locations with its given infrastructure

system to keep the city running. Transferred to the cell, molecular motors carry cargoes on cellular streets to various locations at the proper time to maintain vital functions.

The cellular infrastructure system consists of microtubules and actin filaments. Micro-

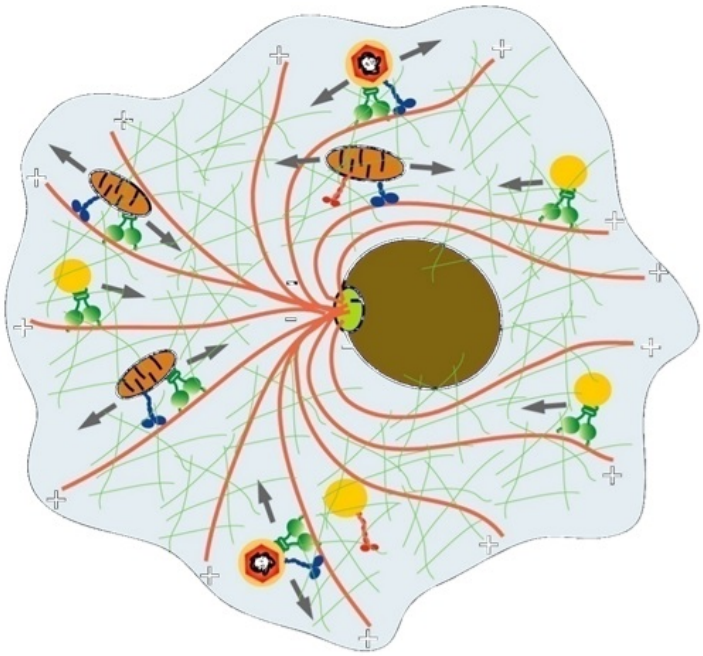

Figure 1.1: Organization of microtubules (red lines) and actin filaments (green mesh) in an eukaryotic cell; microtubules arise from the centrosome (light green) attached to the nucleus (brown); kinesin (blue), dynein (green), myosin (red) carry different forms of cargoes

tubules are polar, with their 'minus end' attached at the centrosome which is situated close to the nucleus and the 'plus end' pointing towards the periphery of the cell. Actin filaments are more randomly oriented and significantly shorter than microtubules. It is assumed that actin filaments build a bridge between microtubules at low microtubule density in a specific region [29]. The specific organization and density of microtubules

and actin filaments is surely dependant on the cell type. While in many mammalian cells and other cell types the microtubules are radially oriented from the cell center towards the periphery of the cell (see figure 1.1), some cells exhibit completely different structures of their microtubule network [29].

1.1.1 Failure of active transport

Active transport inside the cell is a very sensitive mechanism since many different cargoes have to be transported to a myriad of locations in the cell at the same time. Hence, a tight regulatory mechanism is required. Otherwise, failure of this transport system may lead to a lack of certain molecules or organelles at the desired locations and thus malfunctioning of some cellular processes. Impaired transport has been linked to neurodegenerative, mental or developmental diseases like Huntington's, Parkinson's, Fragile X or Alzheimer's disease (AD) [40]. Most of these diseases are linked to failure in regulation of the involved motors. To study the relation between impaired motor regulation and neurodegenerative diseases, the fruit fly, *Drosophila melanogaster*, is a useful model system since, among others, 75% of known human disease genes have a recognizable match in the genome of fruit flies [44].

1.2 Molecular motors

Essentially three different motor families - kinesin, dynein and myosin - conduct active intracellular and neuronal transport. Each of these families has multiple members (in humans for instance, 45 different kinesins, 14-15 dyneins and 40 different myosin

members are present, however cargo transport is done by only some of them [53]). The most significant motors for intracellular transport found in the majority of eucaryotic cells are kinesin-1 (also called conventional kinesin), cytoplasmic dynein and myosin-V (see figure 1.2). In the following, 'kinesin' is used to refer to kinesin-1, 'dynein' to cytoplasmic dynein and 'myosin' to myosin-V.

Kinesin walks towards the plus-end of the microtubule whereas dynein moves inwards

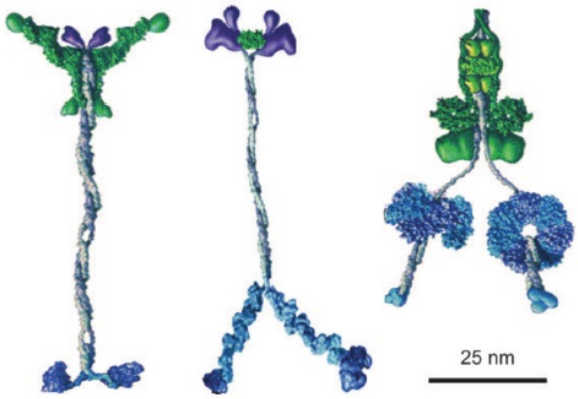

Figure 1.2: Schematic of molecular motors, from left to right: kinesin-I, myosin-V, cytoplasmic dynein (taken from [53])

towards the minus-end. Actin filaments are used by myosin motors to carry cargoes [53] and are not the focus of this thesis work.

Two crucial elements characterize the motors carrying cargoes along microtubules and actin filaments: the motor domain (bottom part of each motor in figure 1.2) and the tail domain (top part of each motor in figure 1.2). The motor domain, also called 'head', performs steps on cytoskeletal tracks while the tail domain binds the cargo. Each of the three motors has two identical 'heads' to perform steps. In myosin and kinesin, there is a single nucleotide binding site for hydrolysing one ATP per head. ATP acts a a fuel

for the motor since the hydrolysis of ATP at the catalytic site induces conformational changes of the motor which results in a motion on the cytoskeletal filament in a stepwise fashion. For each step one ATP gets hydrolyzed, corresponding to a step length of 8 nm for kinesin [46] and 36 nm for myosin [30]. These step lengths match the repeat of the tubulin dimers that build the microtubule and the pseudo-repeat of the actin filament, respectively. The head domains of dynein are more complex. Dynein has multiple ATP binding sites in each head and moves probably by coordination of the two heads accompanied by rotation of the head [29] resulting in step sizes that can be larger than 8 nm. Usually, the multisubunit dynactin complex binds to the cargo binding domain of dynein. Dynactin may bind to several different proteins and thus link dynein to different cellular cargoes [53].

In the majority of eukaryotic cells, there are multiple motors of different families attached to the cargoes. This allows cargoes to be transported on both actin filaments and microtubules [29]. Also, the cargoes can frequently switch between plus-end and minus-end movement on the microtubules. In the next section, possible mechanisms of bidirectional transport along a filament are described.

1.3 Regulation of bidirectional transport

Only little is known about the coordination and regulation of bidirectional motion in most cells since there are probably various co-working mechanisms.

It turns out that two different mechanisms of bidirectional cargo movement are possible: tug-of-war between opposite polarity motors or regulation of opposite polarity motors

attached to the cargo; one kind switched on at a time.

In the tug-of-war model [33], all motors bound to the cargo also attach to the cytoskeletal filament and opposite polarity motors fight against each other like in a tug-of-war. Stochastic binding and unbinding of the motors under opposing force determines the direction of cargo transport.

Recently, tug-of-war between kinesin and dynein was shown *in-vitro* by developing a cargo which controls the numbers of kinesin and dynein attached to it [18]. Cargoes with different ratios of kinesin to dynein motors attached moved mostly unidirectionally along the microtubule which demonstrates that one motor type wins the tug-of-war. Some ensembles with certain kinesin to dynein ratios were nonmotile. Nevertheless, this non-motility was resolved by photocleaving the linkage of on motor type to the cargo. While the tug-of-war is possible to generate in artificial *in-vitro* systems, it was not possible to demonstrate the tug-of-war in *in-vivo* systems. In fact studies investigating the tug-of-war *in-vivo* revealed other possible mechanisms of bidirectional cargo movement [20, 48, 27]. Manipulation of cargoes (lipid droplets) in *Drosophila* embryos was performed using an optical trap [27]. Switching the optical trap on causes the cargo to stall and eventually the motor(s) detach from the microtubule which results in the motor-cargo complex falling back to the center of the trap. Equal numbers of kinesin and dynein were shown to move the lipid droplets, however it was found that it is more likely for the cargo to continue its motion in the original direction after detaching in the optical trap. This contradicts the 'tug-of-war' model for *in-vivo* transport where a cargo is expected to start moving in either direction with equal probability. These findings suggest that only one motor type is active at a time. Thus, the motor-cargo

complex seems to be regulated by molecules or processes inside the cell which trigger the bidirectional motion of the lipid droplet. While the tug-of-war is not used for bidirectional transport, it is possible that the cell takes advantage of the tug-of-war for other processes like vesicle fission [49].

Evidence for proteins that regulate transport are well established in relation to many cargoes. For example, the kinase GSK-3 reduces the activity of both kinesin and dynein and is important for Alzheimer's disease pathology [58]. Lis1 regulates dynein and alters its reaction to loads [31], PKA regulates pigment granule transport in fish melanophores [51]. However, the regulatory events are barely understood on a molecular level. Additionally, many different molecular species can be involved in one regulation process [59].

1.4 Approaches investigating motor regulation

Three complementary approaches address the transport regulation mechanisms. In the 'top-down' approach, one considers cargoes in intact *in-vivo* systems and tries to investigate how a net directed transport is achieved by employing mutants that target the regulatory mechanism. In the 'bottom-up' approach, purified motors are usually attached to artificial cargoes and single molecule *in-vitro* studies can be performed in the absence or presence of regulators. The 'intermediate' approach adds more of the native complexity to the 'bottom-up' approach by using endogenous motor-cargo complexes purified from the cells. The intermediate approach will be investigated in this work, and is sometimes termed '*ex-vivo*' since functional complexes are extracted from the cell.

Ex-vivo experiments typically involve stabilized microtubules attached to a coverslip

and studying transport of purified cargoes with their endogenous motors. Hendricks et al. [24] used purified neuronal transport vesicles to study motor coordination *ex-vivo*. The bidirectional movement of the purified vesicles *ex-vivo* ressembles vesicle motility in neurons. That work also showed that a small number of motors (one to five dynein and one to four kinesin) stayed stably attached during the purification process. Without any regulatory factors in buffer, the motors associated with the cargo can fight against each other when simultaneously engaged. In fact, combining the fast switching between plus- and minus-end directed transport of the purified vesicles and the numbers of motors attached to the cargo, the bidirectional movement correlates well with the theoretical tug-of-war model. Similar unregulated tug-of-war *in vitro* was suggested for lipid droplets purified from *Drosophila* embryos as described in section 3.1.

To tease out the regulation process, these '*ex-vivo*' assays can be supplemented by regulatory proteins that can resolve the tug-of-war and recapitulate the transport inside cells.

1.5 Probing motor regulation *ex-vivo*

To visualize a single regulatory process, one can add the putative regulator to the plain *in-vitro* motility assay. Thus, an *ex-vivo* sample for studying regulation processes would contain microtubules, a motor-cargo complex extracted from a living system and one or multiple species of regulatory molecules.

There are three possibilities where the regulatory molecule can act on to resolve a tug-of-war; for example; The regulator may directly act on the motor and change its activity; the regulator may act on the microtubule and alter motor-microtubule interaction; or

the change in motor activity can be just a byproduct of a process in which the putative regulator is involved. The last scenario is not compatible with *ex-vivo* experiments since this mechanism cannot be observed unless a larger fraction of the complex cellular components are added. A possible scenario for the first case where the regulator acts

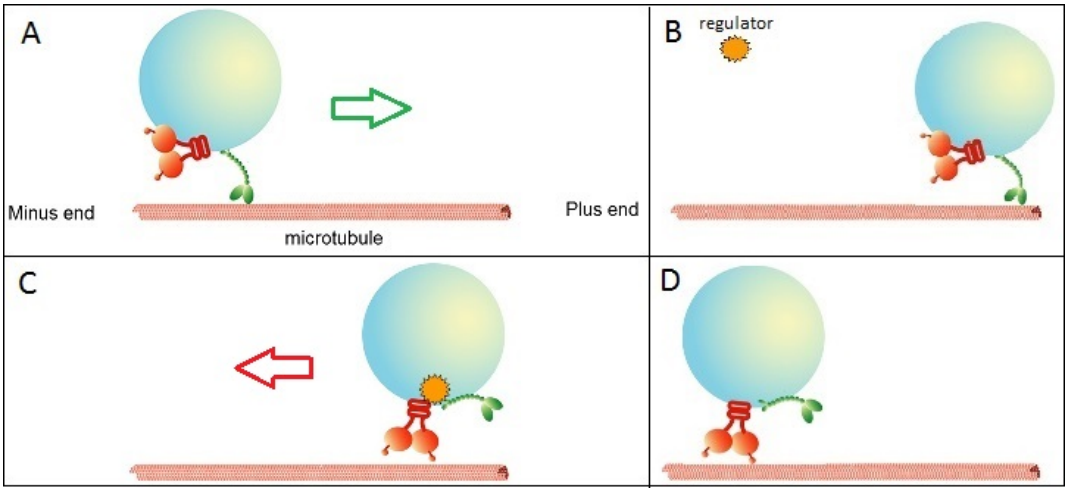

Figure 1.3: Schematic of a possible regulation process to switch direction in an *in-vitro* assay; A: motor-cargo complex (for example lipid droplets or vesicles) has kinesin (green) attached to the microtubule and dynein (red) inactive, which causes a movement to the plus-end of the microtubule; B: after a certain time, a regulator out of solution approaches the motor-cargo complex; C: the regulatory molecule acts directly on the motors. Now dynein is active and kinesin inactive; D: the movement continues now in the minus end direction of the microtubule, the regulator is not shown any more, but can still be attached to one or both motor domains

directly on the motor is shown in figure 1.3 for the case of directionality regulation. Studying this kind of process *ex-vivo* can give insight into the regulation process in the cell and would also be the first step to approach the complexity of a cell. Further, it can allow higher throughput than experiments in cells and does not suffer from potential genetic interactions that can be unavoidable *in-vivo*.

However, imaging such a process where a regulator acts directly on a cargo bound to a microtubule brings along some challenges. Visualizing the regulator, microtubules, the motor-cargo complex as well as manipulating the motor-cargo complex at the same time requires a sophisticated microscope setup [12]. A suitable method to visualize microtubules and the motor-cargo complex is differential interference contrast (DIC) microscopy that enables imaging transparent objects. It is to notice that the motor proteins attached to the cargo generate almost no contrast, therefore only the cargo (usually 200-1000 nm in size) can be seen in the DIC image. The regulatory molecule is too small (usually < 1 nm) to be imaged with DIC microscopy. A common technique to visualize proteins is labelling them with a fluorescent dye or fluorescent protein fusion. To visualize the fluorescent regulator and locating it while bound to the motor-cargo complex, a sensitive fluorescence microscopy is needed. Finally, an optical trap is also required to place the motor-cargo complex above a microtubule so that the motors can attach and probe its mechanical properties.

In the following chapter, a setup that combines these three techniques to study motor regulation is described in more detail. Chapter 3 describes an experiment towards the goal of visualizing such a regulation process with the new microscope setup.

Chapter 2

Setup design and methodology to visualize motor regulation

In this chapter the elements required to image a regulation process and the setup of the microscope are described. We use a "Nikon Ti-U" microscope which is constructed for bright-field and differential interference contrast (DIC) imaging, but modified to allow implementation of optical trapping as well as total internal reflection fluorescence (TIRF) microscopy.

DIC microscopy allows visualizing objects of the size of cellular cargoes and microtubules while the TIRF microscopy can image fluorescently-labelled single molecules. The optical trap permits the manipulation of the motor-cargo system. First the three different components of the microscope - TIRF, DIC and optical trapping - will be described and then the combined setup of these three capabilities will be shown. Subsequently the reasons for modifications of the original setup [12] and the combined setup will be described.

2.1 Total Internal Reflection Fluorescence (TIRF)

As mentioned before, fluorescence microscopy is a suitable method to observe biological processes since it can give contrast specific to the molecule of interest by labelling it

using a fluorophore. The fluorophores get excited by the illumination light, usually by a monochromatic laser with a wavelength that falls within the absorption spectrum of the fluorophore. The fluorescent molecule then emits light which is normally at longer wavelengths compared to the wavelength of the absorbed light due to the Stokes shift. Labelling of the biological molecule of interest happens by either using fluorescent proteins or by chemically attaching an organic or inorganic fluorescent dye like for example Cy3 or Carboxytetramethylrhodamine (TAMRA). To image single molecules, the use of a high sensitivity camera is necessary because the fluorescence intensity of the dye is typically in the order of fW at an excitation intensity of hundreds of W/cm^2, assuming an emission rate of 10000 photons per second [54].

There are several techniques for fluorescence microscopy. In epifluorescence microscopy the excitation light is focused through the objective on the specimen. The emitted light of the fluorophore passes back through the same objective and is separated from the excitation light by a filter. Since the whole sample is illuminated, out-of-focus background fluorescence deteriorates the signal. Detection of a single fluorophore would not be possible [50]. A suitable technique to detect single molecule fluorescence is the total internal reflection fluorescence (TIRF) microscope which only illuminates a thin section of the specimen, thereby eliminating background fluorescence from outside the focal plane. The improved signal-to-noise ratio enhances the spatial resolution of the features of interest [45]. In a through-the-objective TIRF setup, a laser beam gets directed on the sample by the objective at an angle equal to or higher than the critical angle for total reflection of the boundary between glass slide and medium. An evanescent wave penetrates in the sample when light gets totally reflected at the interface of the

two media with different refractive indices. The TIRF excitation laser beam is adjusted so that the evanescent wave decays exponentially with a decay constant of the order of 100 nm which guarantees that the laser only illuminates dyes which lie in a region close to the surface. This enables the visualization of single molecules.

2.2 Differential Interference Contrast (DIC) microscopy

There are several techniques used to obtain contrast in optical microscopy without fluorescent labelling. While for example bright-field microscopy uses absorption as a contrast mechanism, phase contrast microscopy which is also an important method for biological samples utilizes the phase shift of the illumination light when it passes through the sample. Differential interference contrast (DIC) microscopy, however, employs interference of the incoming light split in two parts by a birefringent prism. The main advantage compared to phase contrast microscopy is the use of the full aperture of the objective which leads to a better resolution [28]. Also, the lack of distracting halos is a benefit of DIC.

The general DIC schematic is shown in figure 2.1. The illumination light passes through a polariser to produce plane-polarized light. Then the light enters a Nomarski prism (in figure 2.1 'DIC prism') where the beam is split in two parts, the ordinary (O in figure 2.1) and the extraordinary (E in figure 2.1) beam. The condenser then focuses the two beams so they travel parallel through the specimen and pass two adjacent points in the sample which are separated by less than the resolution of the system [28]. When the two wavefronts pass through the specimen they experience different optical path lengths. The two beams are brought into focus at the rear focal plane by the objective where the

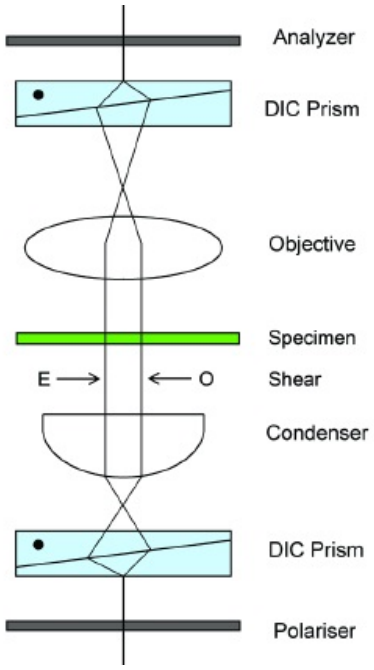

Figure 2.1: Schematic of the optical setup used for DIC microscopy (from [28])

second Nomarski prism aligns the two beams together in a common path. For the two beams to interfere, the analyser brings them in the same polarization plane and axis. This setup results in a shadow effect of objects in the sample which leads to a pseudo three dimensional image.

With the usage of fluorescence and DIC microscopy, the cargoes, microtubules and single molecule regulators can be observed. In addition to that an optical trap is installed to allow the manipulation of the motor-cargo complex.

2.3 Optical Trapping

An optical trap is added to the microscope setup. For the purpose of the present work, it is mainly used to manipulate the cargo bead and position it above a microtubule. Future experiments may require force measurements which the same trap allows by projecting the light scattered by the cargo bead onto a quadrant photodiode to measure displacements.

The method of optical trapping was invented by Arthur Ashkin in the early 1970s [9]. He established a three-dimensional trap which could stably capture micron-sized dielectric particles. An optical trap, also called "optical tweezers", uses a highly focused laser beam due to which micron-sized particles can be trapped in the focus of the beam. With the technique of optical trapping the displacement of micron-sized dielectric particles can be measured with nanometer precision and forces in the order of pN can be applied to the particles simultaneously which can be used for studying transport and force generation of molecular motors.

Today's optical traps work with a highly focused laser beam with an objective of high numerical aperture (NA). A dielectric particle experiences an optical force due to momentum transfer from the scattering of the light. For claritiy reasons, the optical force acting on the particle can be divided in two parts, the scattering force and the intensity gradient force.

First, one can imagine that the photon stream pushes the dielectric particle in the direction of the laser light propagation. The incident light can scatter in various directions or can get absorbed. Thus, the photons transfer momentum to the particle and the resulting force points in the forward direction; all other force components cancel

out.

Usually, the scattering force dominates. But if there is a steep intensity gradient in the laser beam, the second component is not negligible any more. The intensity gradient force is the force that a dipole experiences when it is situated in an inhomogeneous external electric field and points towards the direction of the gradient. Using a center-peaked 3D intensity profile of the laser beam like a Gaussian intensity profile results in a gradient force which points towards the center and thus allows getting a stable trap where the particle is kept slightly above the focus of the laser beam while above means in the direction of the laser light propagation.

The implementation of optical tweezers enables us to trap the motor-cargo complexes which diffuse in solution close to the sample surface and manipulate them.

2.4 Modifications to the original microscope setup

An instrument combining DIC and TIRF microscopies with optical trapping was previously constructed [12]. The orginal setup [12] had a far-red LED light (Thorlabs M735L2-C3, maximum at $\approx$ 735 nm) used for DIC imaging. To test if the far-red DIC light allows imaging microtubules, fluorescent microtubules were prepared so that they can be imaged using both DIC and TIRF. Rhodamine-labelled tubulin (Cytoskeleton, Tubulin labeled with TRITC rhodamine dye, Cat# TL590M) was added to the unlabelled tubulin supernatant (see step 5 Appendix A.1) at a ratio of 1:9. 500 nm plastic beads were flushed into the sample chamber and immobilized on the Poly-L-lysine(PLL)-coated sample surface. The beads facilitate finding the surface in the DIC channel since the microtubules are poorly contrasted. In an aquistion with an exposure time of

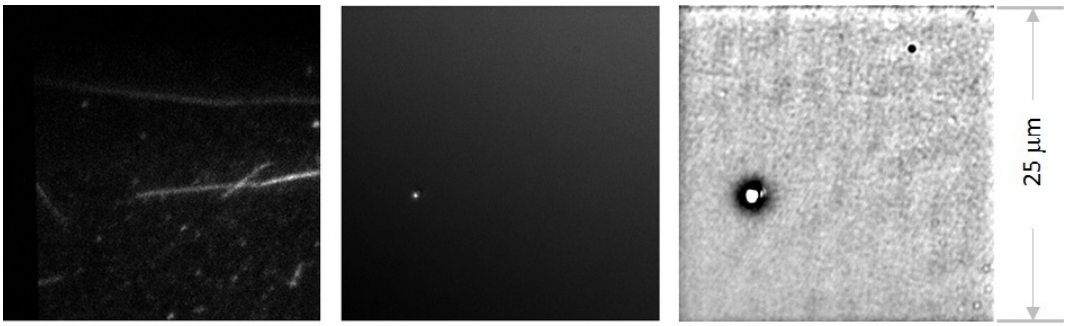

Figure 2.2: Images of microtubules of the same region of interest: a) visible in fluorescence channel of original setup, b) DIC image with far-red light, c) image of 50 frames acquired with DIC, averaged and processed with a FFT-filter implemented in ImageJ

0.036 s, the fluorescent microtubules (see figure 2.2a) are not visible in DIC (figure 2.2b). However, after post-acquisition-averaging of 50 frames and processing in ImageJ [22], microtubules could be made visible (see figure 2.2c). Similar post-processing using a program written in Labview produced comparable results. Hence, I developed a Labview program which performs live-averaging of a preset number of acquired images as well as live processing of the averaged image. The averaged and manipulated image is displayed alongside the live image on a separate screen. Imaging the microtubules at a lower frame rate would not be disadvantageous since the microtubules just have to be visible at the beginning of an acquisition to place the motor-cargo complex on them by means of an optical trap.

However, the Labview functions of acquiring and averaging images are limited. Many functions can only handle 8-bit images which reduces the dynamic range as well as the quality of the processed images. Moreover, the Labview drivers supplied by Andor to acquire the images from the EMCCD result in distorted images with a very limited

pixel value depth, again compromising the image of the microtubules. Finally, Labview was slow in processing the images and slowed down the real-time acquired images. To make the microscope suitable for studying regulation processes, fluorescent events and

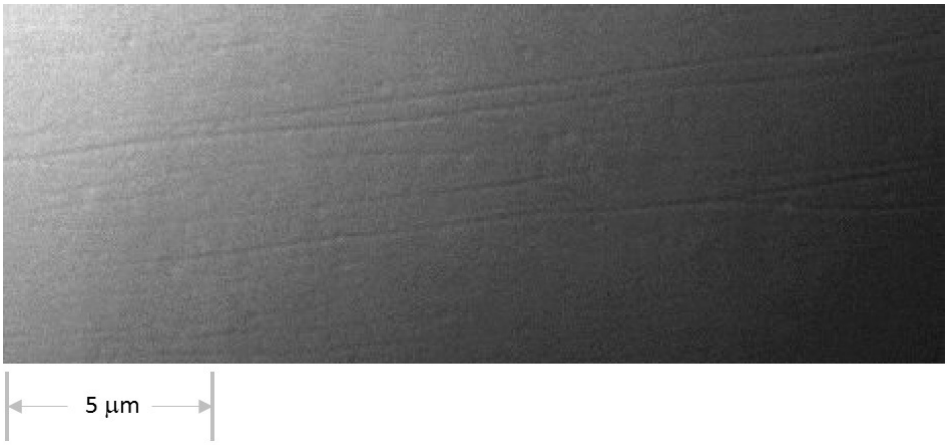

Figure 2.3: Microtubules imaged in DIC with light ranging in wavelength from 565 to 610 nm; exposure time 0.02944 s, no EM Gain

the movement of the motor-cargo complex have to be observed in real time.

To be able to image the microtubules, DIC imaging of a shorter wavelength range was needed. I chose a LED source emitting at 565 - 610 nm. Using this light source the microtubules are visible at an exposure time of 0.02944 s which guarantees real time imaging (figure 2.3). As discussed in subsequent sections, the choice of the DIC light source required further modifications of the setup as well as of the acquisition sequence timing.

2.5 The Combined Setup and Acquisition Timing

2.5.1 Light sources and fluorophore

A 532nm laser (Chrystalaser CL532-100-O, [1]) is used as excitation light for TIRF. This requires the use of fluorophores like TAMRA or Cy3 (see figure 2.4(a) for the spectrum of TAMRA) where the absorption spectrum matches the wavelength of the fluorescence excitation laser.

The DIC light source used is an amber LED light (Thorlabs M590L2-C3) with an emis-

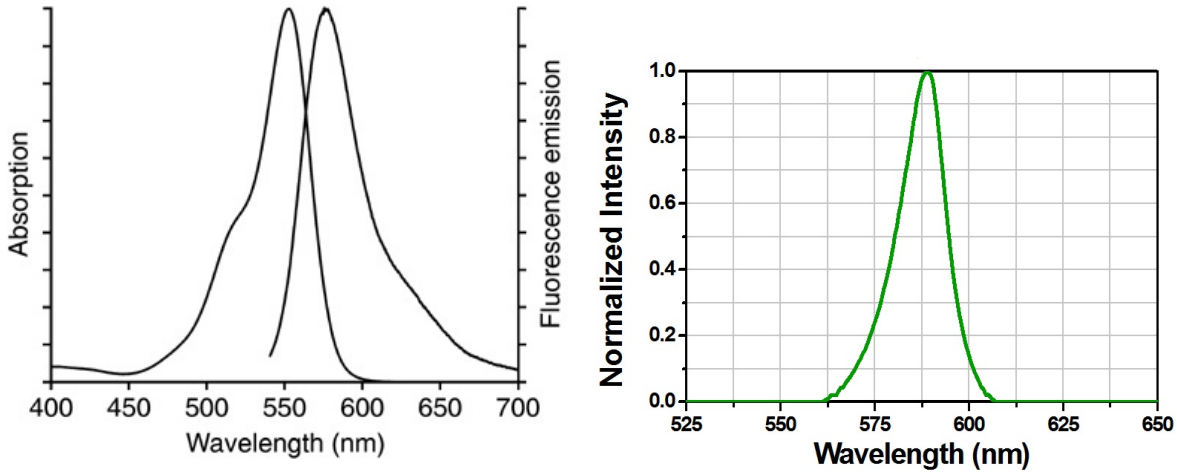

(a) (b)

Figure 2.4: Spectra of (a) normalized absorption and emission of TAMRA dye. Excitation maximum: 545 nm; Emission maximum: 575 nm (taken from [2]); (b): Spectrum of the collimated DIC light source (Thorlabs M590L2-C3)

sion spectrum seen in figure 2.4(b). The wavelength of the optical trap laser (Omicron Laser LDM830.200.CWA.L) was chosen to be 830 nm because it has minimal damage to biological material [35] and doesn't interfere with the wavelength ranges used for TIRF and DIC.

Figure 2.5 schematically shows the wavelength ranges for the various elements implemented in the microscope as well as the absorption and emission spectra of the TAMRA fluorophore which is used as dye in the experiment described in chapter 3. The DIC

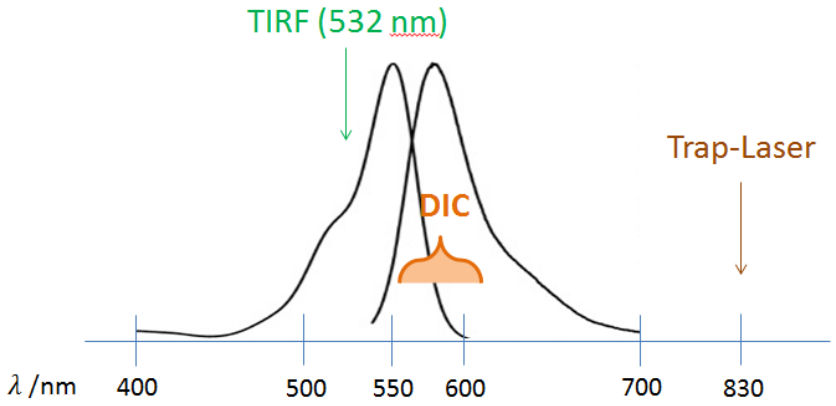

Figure 2.5: Combined schematic of the wavelength ranges of the different microscope components (arb. scale) and absorption/emission spectrum of the TAMRA fluorophore

light slightly leaks into the absorption spectrum of the fluorophore. However, its low intensity compared to the TIRF excitation laser light guarantees that its contribution to excitation and photodamage of the fluorophores is negligible. The schematic also points out that the wavelength range used for DIC coincides with the emission spectrum of the fluorophore which leads to the DIC light and the fluorescence emission being directed into the same camera (Andor iXon+ 897) and necessitate a time sharing scheme to image both (section 2.5.3.2).

2.5.2 Schematic of setup

The setup of the microscope combining TIRF, DIC and optical trapping with all dichroic mirrors and filters is shown in figure 2.6. Here, the correct optical path of the different

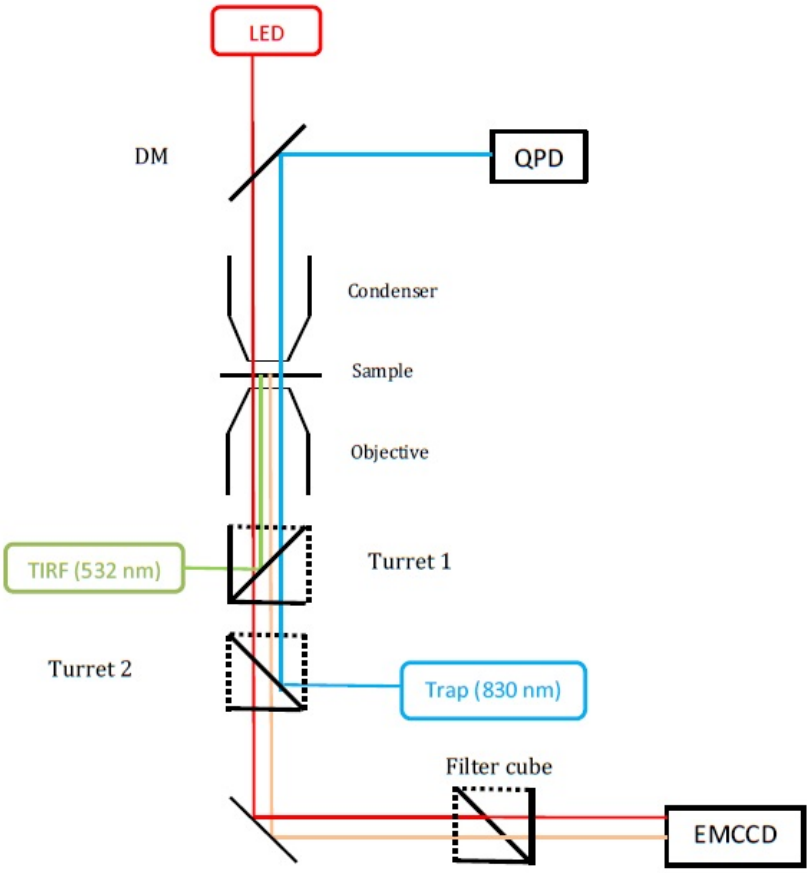

Figure 2.6: Complete microscope setup with DIC, TIRF and optical trapping

beams, the Nomarski prisms, polarizer and analyser for DIC microscopy are not shown for clarity and to emphasize the position and setup of filters, dichroic mirrors, light sources and cameras. The solid lines in the turrets represent filters or dichroic mirrors, the dotted lines indicate that no filters nor other optical devices are placed there and the light passes through completely (see Appendix for specifications of the various components).

The transmission spectra of filters and dichroic mirrors are carefully chosen to guarantee

that only light of the desired wavelength reaches the camera (see [12] for details).

2.5.3 High frequency time sharing-cycle

The fact that both DIC light and fluorescence emission are being directed into the same camera requires to implement a time-sharing mechanism between the fluorescence and DIC signal which can operate at a high frame rate to guarantee real time imaging.

2.5.3.1 Frame-Transfer mode

To reduce the readout time for each frame during an acquisition, the camera is operated in frame-transfer (FT) mode (figure 2.7). In FT mode, the CCD is divided in an equally

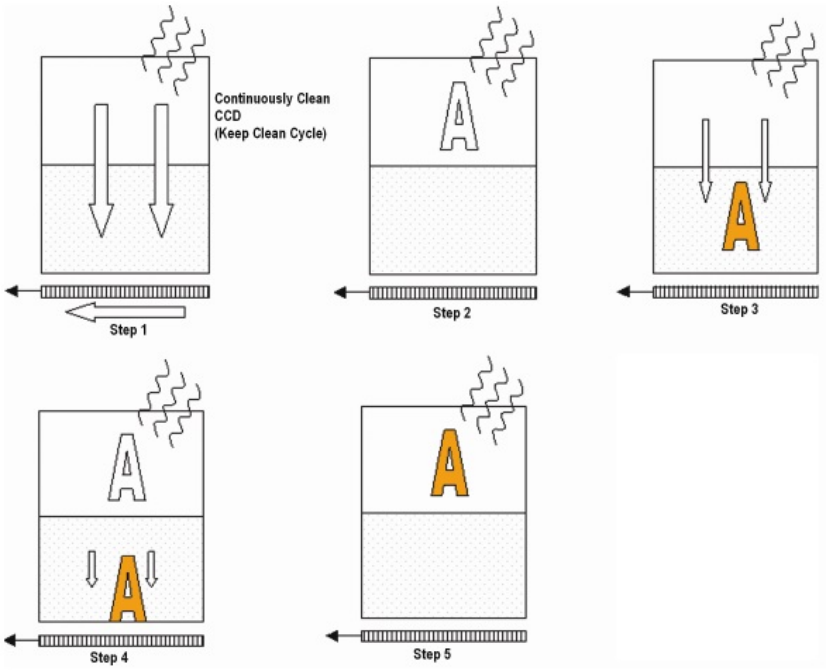

Figure 2.7: Frame-transfer mode of the cooled EMCCD camera (Image courtesy of Andor Technology plc. — andor.com)

sized image and masked storage area. While acquiring an image on the image area, the previous image can be read out in the masked storage area. Thus, no time gets lost between acquiring and reading out the image (see figure 2.7). In step 1, image and storage area are fully cleaned off charge before the acquisition starts. The acquisition starts in step 2, light falls on the image area allowing each pixel of the image area to accumulate charge until the exposure time has elapsed. In step 3, the charge built up in the image area gets vertically shifted into the storage area where in step 4, when the image area is completely shifted in the storage area, vertically shifting stops and charge can build up in the image area again. Meanwhile, the storage area is being read out. After finishing readout, the system waits for the exposure time to elapse and then starts again the readout process (step 5). This mechanism allows the cycle time for acquiring one frame and displaying it be very close to the exposure time and thus allows high frame rate imaging.

One drawback of the frame transfer mode is that the minimum exposure time is restricted to the time taken to read out the image from the storage area which is 0.02945 s when acquiring a kinetic series of the full 512x512 image area. Furthermore, the exposure time determines the kinetic cycle time and cannot be manipulated via software. However, using the minimum exposure time of 0.02945 s still guarantees real time imaging.

2.5.3.2 Time-sharing cycle

Since DIC and fluorescence emission lie in the same wavelength range and are directed into the same camera, a time-sharing mode has to be implemented to trigger between the two signals. The time-sharing cycle is the core of the acquisition process. The cooled

EMCCD camera triggers the digital delay pulse generator (Quantum Composer 9618+) which in turn alternates the status of the DIC light and the TIRF laser. This setting guarantees stable temporal operation since the digital delay pulse generator receives the signal directly from the camera each time a new frame is acquired.

In the time sharing cycle, DIC light and TIRF laser are switched on and off every other frame. The exposure time of each frame was set to 0.02945 s. The cycle time was then 0.03034 s; the additional time originates from vertically shifting the image area in the storage area (see step 3 in figure 2.7). The TIRF laser is switched on for 29 ms. The DIC light is only turned on for 10 ms (see figure 2.8), since the DIC light takes longer to turn off completely and would otherwise leak in the fluorescence channel. Other reasons will be elucidated later (section 3.2). With the chosen settings for the time-sharing

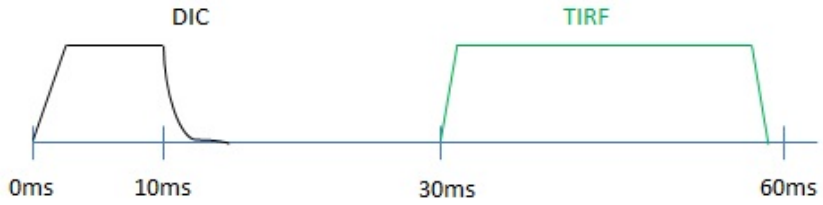

Figure 2.8: Time sharing cycle of acquisition: DIC light is on for 10 ms, TIRF laser for 29 ms

mode, single molecules can be observed in the fluorescence channel. Figure 2.9 shows the intensity graph of a single fluorophore attached to the surface. The increasing and decreasing signal show the start of stimulation of the fluorophore and its photobleaching in the end. The step photobleaching as well as the photon count are characteristic of single molecules.

For the experiment described in the next chapter, the fluorophore attaches to the motor

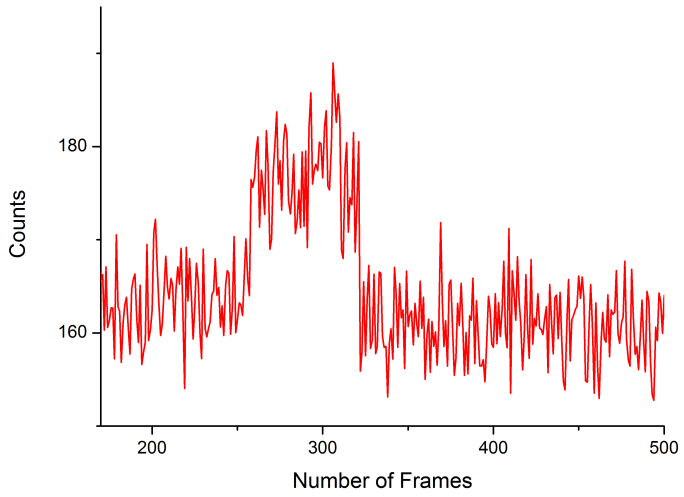

Figure 2.9: Single molecule fluorophore emission and step photobleaching; one frame equals 0.06 s; emission duration is ∼4 s (exposure time of 0.02945 s; EM Gain 150)

head bound to the microtubule which is about a diameter of a single microtubule (25 nm) above the surface. To account for this, the penetration depth for TIRF was adjusted according to the microscope manual which leads to an approximate penetration depth of 80 nm. This guarantees single molecule detection in the proper sample depth and reduced background. The time sharing cycle guarantees the determination of the location of the lipid droplet on the microtubule in the DIC channel and of the fluorescent event in the fluorescence channel.

Before initiating the time-sharing cycle, the DIC Analyser (see figure 2.1) is removed from the beam path to avoid its interference with the fluorescence signal. Imaging immobilized single molecules through the linear polarizer can result in reduction in the collected signal as well as complete disappearance of the signal from fluorophores

whose dipole moments are oriented perpendicular to the polarization direction of the analyser. Removing the Analyser, the presence of the Nomarski prism in the beam path as well as the slightly different wavelengths used for fluorescence and DIC may result in a relative shift of the position of particles when imaged in DIC and TIRF. Such a shift is estimated in the next section.

2.6 Estimation of the Uncertainty of DIC and TIRF colocalization

It is important to demonstrate that the center positions of the particles do not change when the analyser is removed since microtubules are not visible any more after the analyser is pulled out of the beam path. Furthermore, the position of fluorescent objects in fluorescence has to match with its position obtained from DIC. To show this coincidence, large fluorescent objects like fluorescent beads which are also visible in DIC have to be used. Fluorescent beads (Invitrogen, FluoSpheres Carboxylate-Modified Microspheres, 1.0 μm, Nile Red Fluorescent; Cat No. F-8819) whose emission spectrum matches with the one of TAMRA (see figure 2.4(a)), were diluted in buffer and injected into a sample chamber with clean surface. In the following, the DIC setup without analyser is referred to as 'pseudo DIC'. Figure 2.10(a) shows snapshots of fluorescent beads stuck to the surface for the two configurations with and without analyser when either DIC or the fluorescence excitation laser was used to image the beads. The dashed lines illustrate the coincidence of the positions of the different configurations. In addition to that, figure 2.10(b) shows the overlay of two snapshots where both light sources, DIC

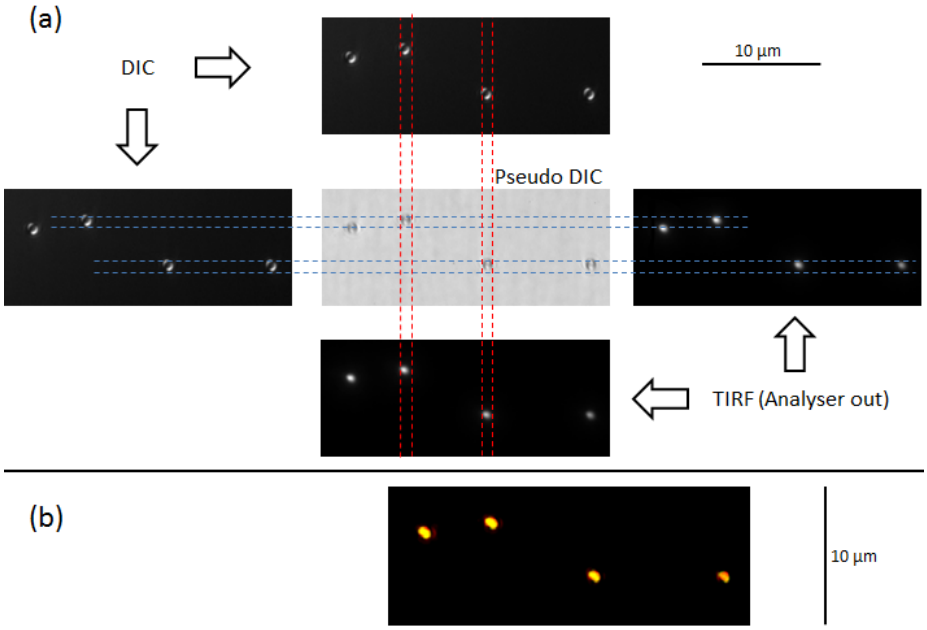

Figure 2.10: (a) Snapshots (exp. time 0.03 s, no EM Gain) of fluorescent beads (1.0 μm in diameter) stuck to the surface of a coverslip in DIC and TIRF with and without analyser show that the positions of the beads in pseudo DIC coincide with both conventional DIC and fluorescence (illustrated with dashed lines); (b) Coloured overlay of snapshots where DIC and the fluorescence excitation laser were switched on simultaneously. Snapshots were manipulated so that the beads were initially coloured green/red for the configuration with/without analyser resulting in a yellow colour in the overlay of the manipulated snapshots

and the fluorescence excitation laser, were switched on simultaneously. The intensities of both DIC and fluorescence are adjusted so that they have similar values. Thus, in our case, snapshots with both light sources switched on is an accompanying powerful tool to demonstrate the coincidence of the positions of the beads. The snapshots (figure 2.10(a)) and the overlay (figure 2.10(b)) demonstrate that the positions of the center of the fluorescence and the center of the beads coincide for both configurations.

To quantitatively estimate the uncertainty in the shift of the image with or without the analyser in the beam path, the center position of ten beads imaged in DIC and in TIRF with and without analyser were calculated. The center position of the beads in pseudo DIC cannot be determined because of distortion of the image contrast due to the missing analyser. By comparing the center positions of the TIRF snapshots, the uncertainty due to removing the analyser can be estimated. By implication, the shift of DIC and pseudo DIC is assumed to be the same since the difference between the typical wavelengths used in DIC and for fluorescence emission (575 nm for TAMRA (see figure 2.4(a)) and fluorescent beads [2]; 590 nm for the LED (see figure 2.4(b)) is negligibly small. In the following, the methods of determining the center position in the different imaging techniques, DIC and TIRF, are described and the results compared.

The beads were imaged in DIC using the maximum extinction mode where the transmission axis of analyser and polariser are crossed. In the maximum extinction mode, the intensity amplitude of a spherical particle along the shear axis is maximal at its edge while it is minimal in its center [3]. However, by just considering the minimum of the intensity profile of the bead along the shear axis, it is not possible to determine both x- and y-coordinate of the center of the bead. To be able to estimate both coordinates of the center position of the bead, the intensity profile of the bead along the x- and y-direction can be used (see figure 2.11). The contrast difference between bead and background along x- and y-direction is still high enough to clearly identify the minimum between the high intensity values at the edge of the bead. An error of 1 pixel is assumed to account for possible uncertainties when determining the pixel value of the minimum in the intensity graph.

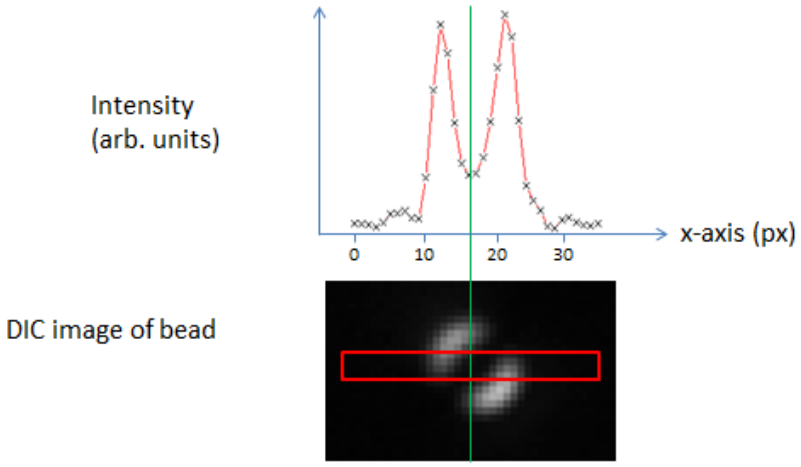

Figure 2.11: Schematic of determining the center position of a bead in the DIC image: An intensity profile is plotted along an area (red) to estimate the center position in x-direction while the height was adjusted so that it approximately lies in the supposed center. The minimum marks the center position of the bead, x_0. Crosses (black) represent the average intensity value for a fixed x in the selected area. The center position of the bead in the y-direction is obtained in a similar way as for the x-direction, along a vertical line (green) fixed at x_0.

Determining the center position of the sphere in the TIRF image with and without Analyser follows subsequent considerations. The emission signal of the fluorophore has to pass the optical setup used for DIC microscopy on its way to the EMCCD camera. This implies that the fluorescent signal of the bead is split by the Nomarski prism into two beams with equal properties but orthogonal polarizations which are shifted along the shear axis (red line in figure 2.12(a)). It cannot be concluded from the manufacturer manual whether the intensity peak of one of the two split beams (figure 2.12(b) in black) or both (figure 2.12(b) in red) indicate the center. Thus, it is reasonable to assume that the center position of the bead is given by the middle of the peaks of the two split beams.

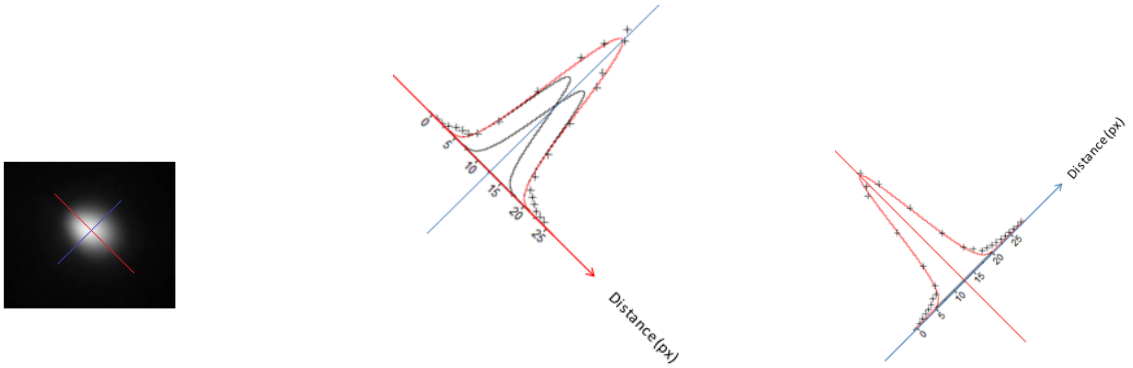

(a) (b) (c)

Figure 2.12: The uncertainty in determining the center position in the TIRF image (a) of a 1μm sphere. The shear axis is shown in red and the axis perpendicular to it in blue. (b) Two single Gaussian curves (black) are fitted to the pixel values (cross) along the shear axis with the same height and width representing the fluorescent signal being split into two beams when travelling through the Nomarski prism. Their superposition is shown in red. The axis perpendicular to the shear axis (blue) passes through the center of the red curve. A Gaussian curve is fitted (c) along this axis.

The center position of the bead in the fluorescence channel was estimated by fitting a 2D Gaussian to the area around the bead with the peak being the center position of the bead. The uncertainty of this method can be determined in two different ways. First, the offset of the peaks of the split beams along the shear axis can be used since it is not clear from the microscope manual how the fluorescent signal gets split in the Nomarski prism. The offset of the peaks of the two split beams was calculated for ten beads and the average was 0.50 pixels. Another measure of the uncertainty of the above described method is considering the difference of the position of the peak of the superposition of the two Gaussian curves along the shear axis (see red curve in figure 2.12(b)) and the peak of the Gaussian-shaped curve fitted along the axis at a 90° angle to the shear axis

(see figure 2.12(c)). The average difference of the two peaks is (0.32 pixels in x- and -0.45 in y-direction) and lies within the average offset of the two peaks along the shear axis (0.50 pixels). Thus, the center position of the fluorescent beads in the fluorescence channel can be estimated with 0.50 pixels uncertainty in each direction.

Figure 2.13 shows the difference of the estimated center positions of the ten analysed fluorescent beads when imaged in DIC, TIRF and TIRF without analyser. No systematic shift can be observed when comparing the difference of center positions estimated for TIRF, DIC and TIRF without Analyser. Further, the average of the difference of the beads' estimated center positions when imaged in TIRF, DIC and TIRF without Analyser lies well within the uncertainties of the above described methods to determine the bead's center.

In the next chapter, the suitability of the microscope setup to observe regulation processes is tested.

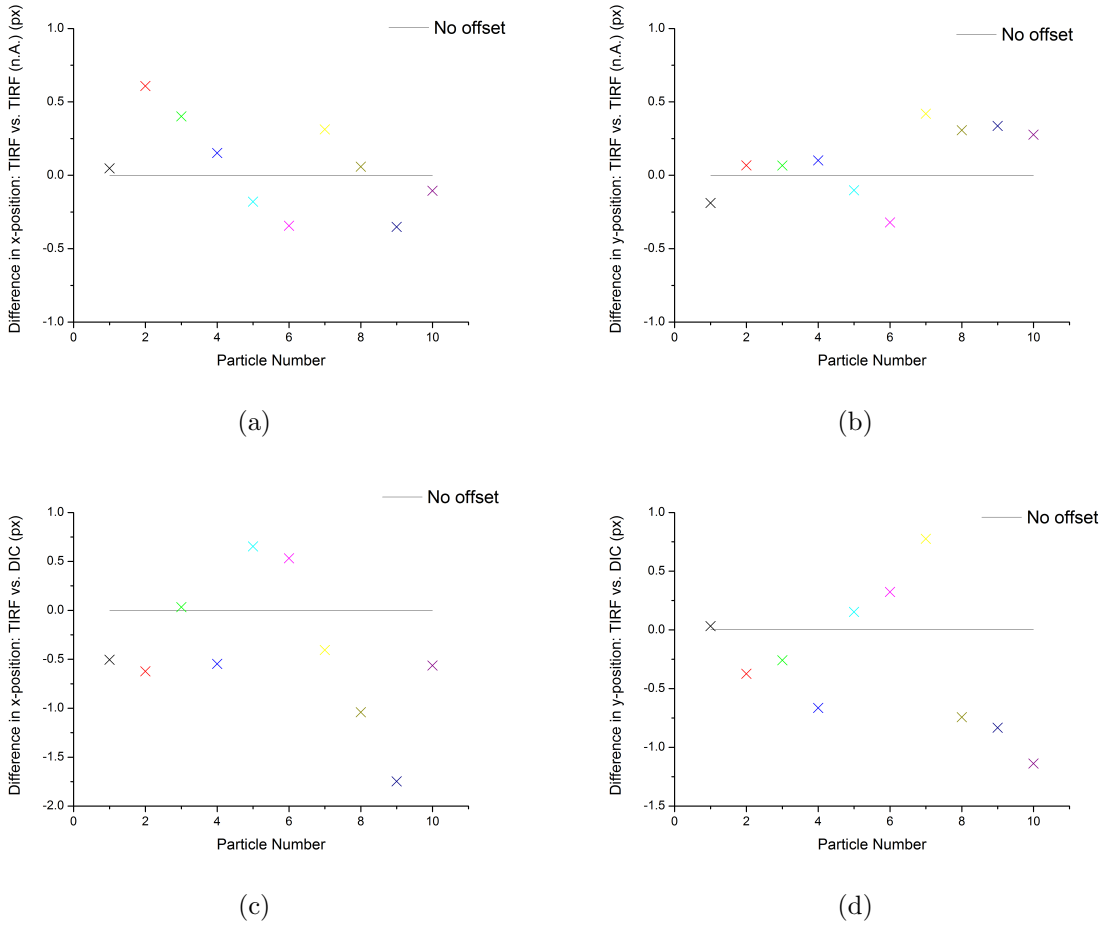

Figure 2.13: Difference of estimated center positions of ten fluorescent beads imaged in TIRF and TIRF with no Analyser (TIRF (n.A.)) in x- (a) and y-direction (b); difference of estimated center positions of the same fluorescent beads imaged in TIRF and DIC in x- (c) and y-direction (d). The solid black line indicates no offset. Crosses with the same color represent the same bead.

Chapter 3

Visualizing a static regulation process

A proof-of-principle experiment was designed to demonstrate the ability of the setup to visualize the regulation process schematized in figure 1.3. Unlike a regulatory protein that may bind transiently with the motors, we chose a simpler case where the fluorescently-labelled molecule binds the motor for a long time. Fluorescently-labelled AMPPNP, a non-hydrolyzable analogue of ATP, was used since it binds to the motor's catalytic domain for an extended time. We used AMPPNP in conjunction with a cargo, lipid droplets, purified from live *Drosophila* embryos with their motors attached. In addition to serving as a test sample for the microscope setup, the choice of lipid droplets allows addressing pertinent questions about the activity of the motor proteins bound to the droplets as described in the next section.

At first an overview of previous experiments [11] on this endogenous motor-cargo complex will be given with implications on the experiment of this work. Then the steps of the acquisition process are explained followed by the analysis of the acquired data.

3.1 Motility of purified lipid droplets *in vitro*

The following is a summary of previous work [11] that examined motor transport of lipid droplets purified from Drosophila embryos. Lipid droplets were purified as described in Appendix A.2, which is the same method used for this thesis work. To confirm that the purification process retained the motors and motor-cofactors bound to the

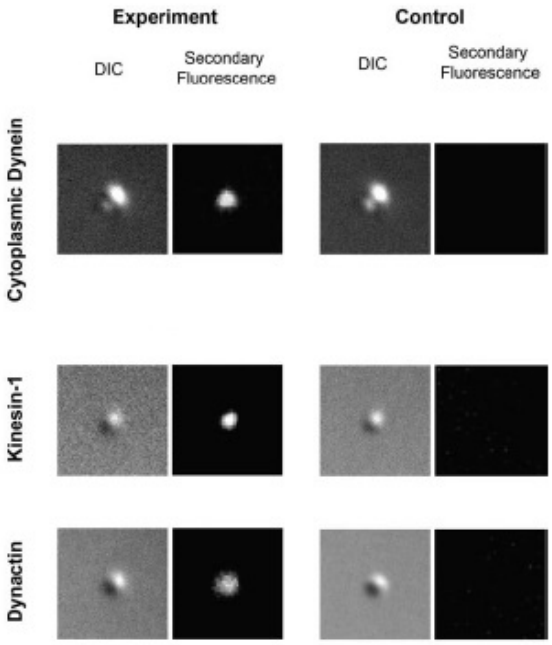

Figure 3.1: DIC and immuno-fluorescence images taken with microscope setup [12] show that motors and cofactors stay attached to the lipid droplet after purification; left: upper panel: fluorescent signal of secondary attached to primary kinesin antibody coincides with position of lipid droplet; middle panel: fluorescent signal of secondary attached to primary dynein antibody coincides with position of lipid droplet; lower panel: fluorescent signal of secondary attached to primary dynactin antibody coincides with position of lipid droplet; right: control with only the secondary in the buffer shows no fluorescence for kinesin, dynein and dynactin

lipid droplet cargoes, lipid droplets were incubated with primary antibodies specific to kinesin, dynein and the dynactin complex and a second fluorescent antibody specific to the primary antibody. Fluorescent spots could be observed for kinesin, dynein and dynactin coinciding with the position of the lipid droplet while in the control experiment with no primary, but only the secondary, no coinciding fluorescence was found (figure 3.1). This demonstrates that the motors-dynactin complex stays attached to the lipid droplets during the purification process.

When the lipid droplets were placed on a microtubule and attached, in very few cases, the lipid droplet started to move long distances along the microtubule. However, in

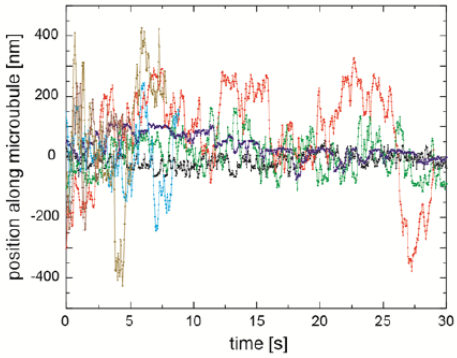

Figure 3.2: Position versus time plot of seven lipid droplets (different color for each droplet) bound to a microtubule. The lipid droplets were recorded by single particle tracking from videos acquired at 30 fps. Short-range back-and-forth motion can be observed for an extended period of time. The amplitude of the back-and-forth motion of the lipid droplets along a microtubule does not exceed a few hundred nanometers. (taken from [11])

most of the cases, the lipid droplet moved a few hundred nanometers back and forth on the microtubule without moving long distances (figure 3.2). While the first observation shows that the motors remained functional, the second observation raises new questions.

The motors might not be active and the lipid droplet binds in another way to the microtubule. The back-and-forth motion would then result from diffusion of the tethered lipid droplet. A more likely scenario is that the motors are active but that the opposite polarity motors, kinesin and dynein, start fighting (tug-of-war) in the absence of any regulators in the purified system. An observation consistent with the latter scenario is that high resolution and high bandwidth position measurements of the droplets using an optical trap revealed detachment of a tether prior to the onset of transport. While this is suggestive of a tug-of-war, direct evidence is still lacking.

The following sections describe an experiment designed to directly probe the activity of the motors by monitoring the binding of fluorescently-labelled AMPPNP. This non-hydrolyzable analogue of ATP binds to the motors only if they are microtubule-bound, thus active, even when the lipid droplet does not move long distances.

3.1.1 Description of the experiment

In my experiment, I use lipid droplets purified from Drosophila embryos the same way as in [11]. A lipid droplet in the assay chamber is brought above a microtubule using the optical trap. The lipid droplet is manipulated so that it attaches to the microtubule whereupon the trap is turned off. The lipid droplet stays on the microtubule diffusing around its anchors. A small concentration (5 nM) of fluorescently labelled AMPPNP molecules is available in the buffer. The nucleotide in the buffer binds to the motor of the lipid droplet cargo only if the motor is one of the anchors which means it is actively attached to the microtubule [52, 14]. A fluorescent spot whose position coincides with the position of the lipid droplet on the microtubule then indicates that the AMPPNP

attached to the motor.

To make sure that only AMPPNP attaches to the motor, no ATP is added to the solution in this experiment since both AMPPNP and ATP attach at the same nucleotide binding site of the motor domain and would thus act competitively. Previous experiments show that at saturation concentrations of ATP and different AMPPNP concentrations the time of the paused AMPPNP state follows an exponential decay with a decay constant of ∼0.5 s and is independent of the AMPPNP concentration [57]. Without ATP, there is no fuel for the motors to walk, thus no long-range motility can occur. Moreover, no competitor for AMPPNP is present suggesting that it is more likely to bind for a longer amount of time to the head of a microtubule-bound motor. Thus, it is reasonable to assume that without competing ATP, AMPPNP should remain at the same spot for at least 0.5 s to be distinguished as bound to the motor.

The mean square displacement (MSD) for a freely diffusing AMPPNP particle in 0.5 s was calculated to verify that the mean distance travelled by a free AMPPNP is much higher than the small diffusion experienced by an AMPPNP molecule attached to a static particle like the motor on the microtubule. The MSD in three dimensions is given by $<x^2> = 6Dt$ where D is the diffusion constant and t the time. The diffusion constant D was calculated for a spherical particle 1 nm in size diffusing in water at T=298K which leads to D = $2.45 \cdot 10^{-10} \frac{m^2}{s}$. In 0.5 s, the particle travels a mean distance of $\sqrt{< x^2 >}$=27 μm. This corresponds to $\sim$ 300 pixels in the image area. Thus, in a timespan of 0.5 s a diffusing particle cannot be mistaken with a static particle. A fluorescent spot at a fixed position for 0.5 s can only originate from particles attached to a static object.

3.2 Imaging the regulation process

Lipid droplet purification, microtubule polymerization and motility sample preparation are described in Appendices A and B. Recording the motility of lipid droplets *in vitro* proceeds as follows: first, imaging in DIC, the surface to which the microtubules are attached is brought into focus and a diffusing lipid droplet is caught from the buffer right above the surface using the optical trap. Next, the droplet is manipulated to bind to one of the microtubules after which the trap is switched off. In the current experiment, the same camera is used to image the lipid droplet cargo as well as the fluorescence of the nucleotide binding to the motor head in the time sharing mode described in section 2.5.2.2. As described in section 2.6, the analyser used for DIC microscopy is removed before initiating the time-sharing cycle. This can be performed manually since the lipid droplet, once bound to the microtubule, stays within a few hundred nanometers of its original position for an extended period of time. Automation, or alternative designs

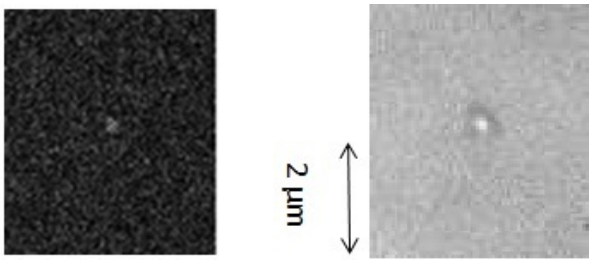

Figure 3.3: TIRF (left) and pseudo DIC (right) snapshots of a fluorophore attached at the position of a lipid droplet (exposure time 0.029 s, EM Gain 150; TIRF channel 5 frames averaged; DIC channel 10 frames averaged)

might need to be implemented in the future for experiments where the cargo starts moving once microtubule-bound. Removing the analyser, however, results in the DIC image losing its pseudo 3D shadow effect. The lipid droplets, but not microtubules, are still clearly visible with this setup (figure 3.3).

The same EMCCD camera images the faint fluorescence as well as the intense DIC

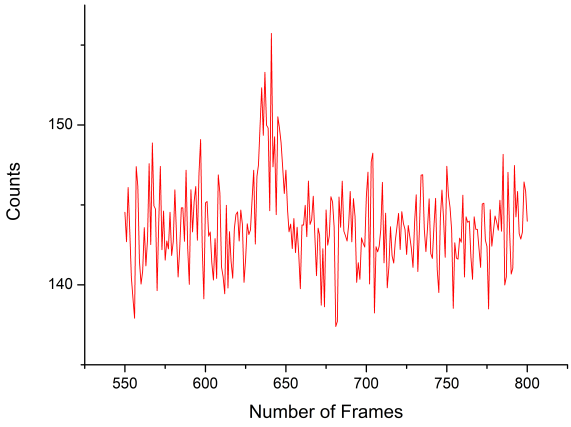

Figure 3.4: Intensity graph of fluorescent spot from figure 3.3: peak around frame 640 shows fluorescent event for $\sim$ 1.1 s; one frame is 0.06 s;

image. A high EM Gain of 150 has to be applied in our experiment to visualize single fluorophore emission. To avoid saturation damage to the EMCCD, the DIC light is only turned on at low intensity for 10 ms out of the 60 ms cycle, while the fluorescence excitation laser is turned on for 29 ms (see section 2.5.2.2 and figure 2.8).

Lipid droplet motility was recorded in video segments of 1 minute duration. Typically 6 videos were recorded for individual droplets. This was necessary due to internal memory limitations of the computer. However, given the small concentration of AMPPNP, the

likelihood of an AMPPNP binding at the catalytic site of the motor head in the time between the end of one video segment and the beginning of the next is negligible as described in the following sections. Figure 3.3 shows a snapshot of a video record of lipid droplet motility both in fluorescence and in pseudo DIC. The image clearly shows a fluorescent molecule localized at the position of the lipid droplet. The corresponding intensity graph (figure 3.4) of the fluorescent spot in figure 3.3 shows a peak which indicates that the fluorophore appeared for ca. 1.1 s.

3.3 Analysis of the AMPPNP binding events

Data was acquired for 57 lipid droplets which attached to a microtubule. To identify which of those colocalized with an AMPPNP molecule in the fluorescence channel, an area surrounding the lipid droplet had to be defined where the motor heads could potentially be. To simplify the analysis, an overestimated area of 14x10 pixels ($\sim$ 1.4x1 μm) was first used to identify potential events which were consequently carefully analysed to identify those which lie in a smaller area of 13x5 pixels that defines where the motor can be (see figure 3.5). The following considerations were used in choosing the areas. For a lipid droplet of radius r tethered to a microtubule, the head of a 100 nm motor can be at most (r + 100 nm) away from the center of the lipid droplet in either direction. This serves as an overestimate as it does not account for the curvature of the spherical lipid droplet. The lipid droplet can diffuse around the tether or shift its center position due to successive binding of multiple motors to the microtubule. To quantify the variation in the center position of a lipid droplet, representative lipid droplets were tracked in the video records using a correlation-based method [16]. Figure 3.6 shows that the center of

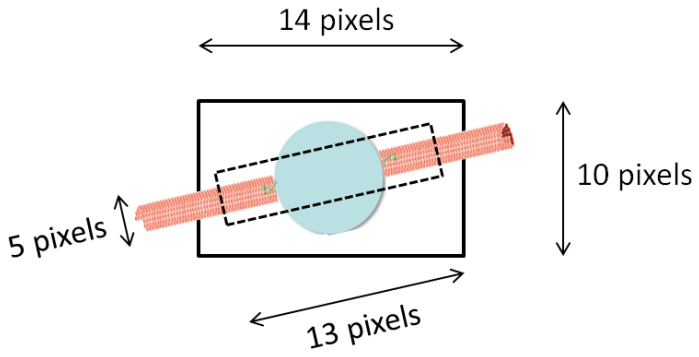

Figure 3.5: Schematic of the area chosen to determine the colocalization of fluorescent spots with the lipid droplet. A large 14x10 pixel area (solid) is used for a quick search for potential events in a video segment where a diffusing lipid droplet is tethered to a microtubule. A fluorescent spot which occurs in a 13x5 pixel area (dashed) oriented along the microtubule with the lipid droplet in its center was counted as a specific attachment of an AMPPNP to a motor head. The microtubule is schematically shown in red, the lipid droplet in blue and the kinesin motor in green

the droplets can span ∼400 nm along the microtubule within a 60s period. Thus, for the lipid droplet averaging in radius 325 nm [11], the fluorescent AMPPNP molecule can lie within a distance equal to $[2 \cdot (325 + 100) + 400]$ nm = 1250 nm surrounding the lipid droplet. This is equivalent to $\sim$ 13 pixels in our microscope image. For the first quick search an overestimated area of 14 pixels long was used. To determine the width of the area where the motor head can be, we measured the thickness of the microtubules in the DIC images. The thickness was 3 pixels (∼300 nm) as expected due to diffraction. While the motor head (and consequently the AMPPNP molecule) can only be bound to the 25 nm diameter microtubule, the shadowed image of the microtubule in DIC did not allow determining its precise position. However, since the goal if this analysis is in determining an upper bound of the percentage of AMPPNP molecules colocalizing

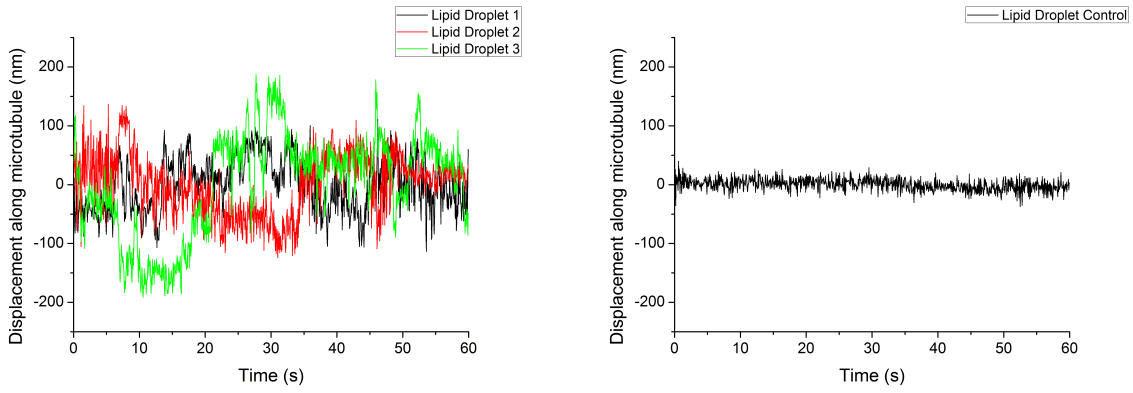

(a) (b)

Figure 3.6: Displacement of three lipid droplets (a) tethered to a microtubule show a maximum of 400 nm displacement along the microtubule. In the control (b), a lipid droplet was tracked while stuck to the surface. The small displacement in (b) suggests that the lipid droplets in (a) were indeed tethered by the motors

with the motors, we used an area $3 + 2 = 5$ pixels wide to account for the perceived width of the microtubule as well as the uncertainty in the coincidence of the fluorescence and DIC images before and after removing the analyser, discussed in section 2.3. This results in an area of 13x5 pixels around the lipid droplet where the fluorescence molecule can be counted as colocalizing with a motor head. For the initial quick search, a width of 10 pixels was used to account for a possible tilt of the microtubules with respect to the field of view (e.g. figure 3.5). For all events identified in the large 14x10 pixel areas, the orientation of the refined 13x5 pixel area was aligned with the orientation of the microtubule, and only fluorescent spots occuring within the refined area were counted as specific events.

For the 57 microtubule-bound lipid droplets recorded in 249 one-minute video segments ($\sim$ 4 video segments/lipid droplet in average), 44 fluorescent spots could be observed in

the selected 14x10 pixel areas. Thus, the mean time it takes to observe a fluorophore in the 14x10 pixel area is 340 s.

Some of the tethered lipid droplets released from the microtubule after a very short amount of time (< 40 s). For these 17 short-time attached lipid droplets, no fluorescent spot appeared while microtubule-bound. This is not surprising since the mean time it takes for a fluorescent spot to appear in a 14x10 pixel area is 340 s. Hence, the 17 lipid droplets that attached for only a short time were not used in further analysis. Thus 44 fluorescent spots were detected for 40 lipid droplets that attached for a long time ($>$ 200 s; 232 video segments; 5.8 video segments/lipid droplet in average).

Out of the 44 fluorescent spots, 15 'events' could be identified as colocalizing with the motor head as defined by the above described 13x5 pixel 'event' area. No accumulation of fluorophores was observed at non-microtubule bound lipid droplets. Dividing the number of 'events' by the number of lipid droplets leads to an average of 38% of the lipid droplets colocalizing with an AMPPNP molecule.

3.4 Unspecific AMPPNP attachment to the surface

Despite blocking the surface with casein to minimize non-specific attachment, there was a certain amount of fluorescent AMPPNP randomly attached to the surface of the coverslip at positions that do not coincide with the lipid droplets (see figure 3.7). This raises the possibility that fluorophores at lipid droplet positions could be bound non-specifically. For unspecific attachment to be discounted, the attachment rate of AMPPNP at the lipid droplet has to be significantly higher than the unspecific attachment rate at the surface. To measure the attachment rate of AMPPNP to the surface a step detection

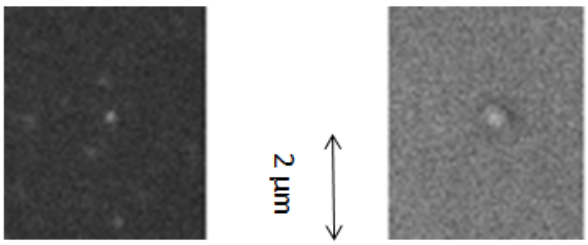

Figure 3.7: TIRF (left) and pseudo DIC (right) images showing an AMPPNP molecule attached to the position of a lipid droplet (bright spot) as well as other AMPPNP molecules binding the surface at other locations (exposure time 0.29 s, EM Gain 150; TIRF channel 50 frames averaged; DIC channel 10 frames averaged)

algorithm was implemented to detect step-like intensity increases due to fluorophore emission in random 14x10 pixel areas not associated with a lipid droplet.

3.4.1 Step Detection Algorithm

I adapted and modified the step detection algorithm described in [37] for the purpose of detecting narrow steps of short duration as seen in figure 3.4. In the following I briefly describe the algorithm.

The time series is first preprocessed by convolution with a Gaussian kernel with standard deviation σ which smoothens the data. A window of width 2w with middle point i is selected out of the processed time series with length N (N > 2w). A piecewise linear fit f_i with uniform slope is performed for the left and right half of the window (see figure 3.8)

$$f_i(x_j) = \begin{cases} m_i x_j + t_i^l & \text{for } i - w < j < i - 1 \\ m_i x_j + t_i^r & \text{for } i \leq j < i + w \end{cases} \tag{3.1}$$

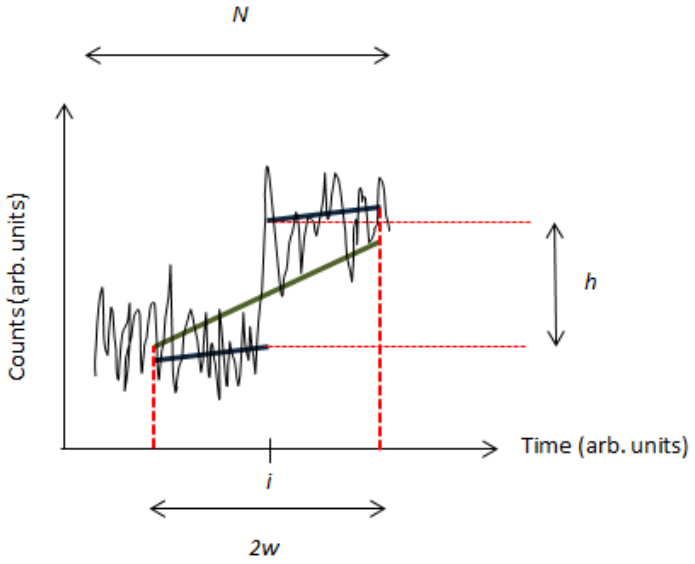

Figure 3.8: Schematic of the step detection algorithm: In a moving window of length 2w and center position i a piecewise linear fit $f_i(x_i)$ (blue) with uniform slope and a linear function $g_i(x_i)$ (green) is fitted to the preprocessed time series of length N (N > 2w). The difference in the residual sum squared of both fits is an indicator for a possible step occurring in that window

In the same window i-w $\leq$ j < i+w, a continuous linear function g_i is fitted with the least square method:

$$g_i(x_j) = m_i^0 x_j + t_i^0 \text{ for } i - w \leq j < i + w \tag{3.2}$$

The optimal free parameters for the piecewise linear fit are obtained by simple linear regression which minimizes the sum of squared residuals. The slope and intercepts are

given by

$$m_i = \frac{w \sum_{j=i-w}^{i+w-1} x_j y_j - \left(\sum_{j=i-w}^{i-1} x_j\right)\left(\sum_{j=i-w}^{i-1} y_j\right) - \left(\sum_{j=i}^{i+w-1} x_j\right)\left(\sum_{j=i}^{i+w-1} y_j\right)}{w \sum_{j=i-w}^{i+w-1} x_j^2 - \left(\sum_{j=i-w}^{i-1} x_j\right)^2 - \left(\sum_{j=i}^{i+w-1} x_j\right)^2} \tag{3.3}$$

and

$$t_i^l = \frac{1}{w}\left(\sum_{j=i-w}^{i-1} y_j - m_i \sum_{j=i-w}^{i-1} x_j\right) \tag{3.4}$$

$$t_i^r = \frac{1}{w}\left(\sum_{j=i}^{i+w-1} y_j - m_i \sum_{j=i}^{i+w-1} x_j\right) \tag{3.5}$$

To cover the whole time series, the window moves through the data and i takes the values w $\leq$ i $<$ N-w. For each window, the residual sum of squares (RSS)

$$\mathrm{RSS}(p_i) = \sum_{j=i-w}^{i+w-1} |p_i(x_j) - y_j|^2 \tag{3.6}$$

is calculated for both $p_i = \mathrm{f}_i$ and $p_i = \mathrm{g}_i$. The difference

$$\theta_i = (\mathrm{RSS}(g_i) - \mathrm{RSS}(f_i))(t_i^r - t_i^l) \tag{3.7}$$

gives a measure of how likely a step occurs at position i, the middle of the moving window. The multiplication with the height of the step $\mathrm{h}_i = \mathrm{t}_i^r$ - t_i^l guarantees that only a step-wise increase of the intensity gets detected by the algorithm. The position i where the value of θ_i is above a certain threshold γ is then regarded as a step.

In this model, the free parameters σ, w and γ are optimized by applying the algorithm on simulated time series where noise amplitude, step height and step length resemble the real data closely.

3.4.1.1 Choice of Parameters

Three groups of 100 data sets were simulated with Labview. Uniform white noise with amplitude 10 was added to a step function of 1000 data points with step height 4. The length of the step was chosen to be 20, 40 and 100 data points for each simulated group of data sets which corresponds to a time of 1.2 s, 2.4 s and 6 s in the real time series. Figure 3.9(a) compares the intensity of a simulated signal with the intensity graph

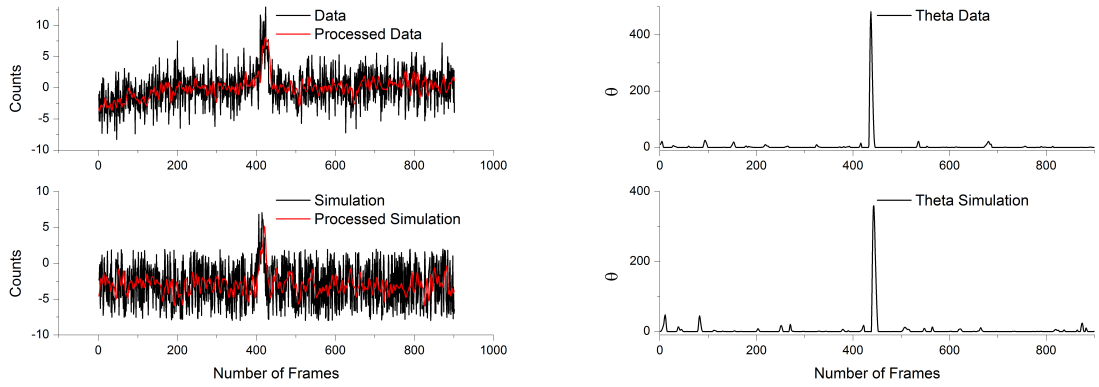

(a) (b)

Figure 3.9: (a) upper panel: intensity graph of a fluorescent spot appearing at a lipid droplet position in a 14x10 pixel area (black) convoluted with a Gaussian kernel with $\sigma = 1.6$ (red); lower panel: simulated signal (step height 4, noise amplitude 10, step length 20) in black, convoluted with a Gaussian kernel with $\sigma = 1.6$ (red); (b): resulting θ values by applying the step detection algorithm (2w = 48) on the preprocessed data

obtained for an AMPPNP molecule as well as the processed data before applying the algorithm. Both graphs show almost identical noise, step height and step length. Figure 3.9(b) shows the result of the step detection algorithm applied on the preprocessed data. A threshold of $\gamma = 100$ was used to identify steps from θ values. The peak coincides with the step-like intensity increase of the preprocessed signal. The step lengths of

the fluorescent spots at the position of the lipid droplet are typically small; between 20 and 40 data points. Thus, more weight is placed on the simulated group with the shorter step lengths when choosing the free parameters σ, w and γ. In chosing these parameters the goal is to maximize the detection rate of the steps while minimizing the 'false positives'. Figures 3.10 and 3.11 show the 'detection rates' and 'false positives' when two free parameters were fixed while varying the third. The 'detection rate' is the

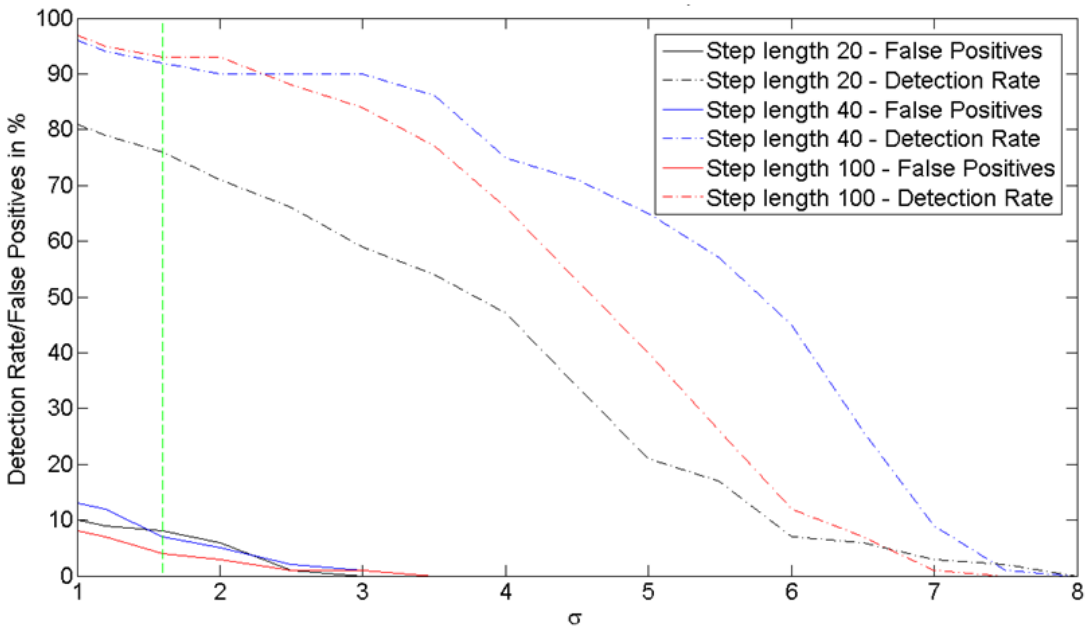

Figure 3.10: The detection rate and the percentage of detected false positives as a function of the width of the Gaussian smoothing kernel σ. The rates drop monotonically for step lengths of 20, 40 and 100 frames. 2w = 48, $\gamma = 100$

percentage of values with $\theta_i > \gamma$ located at the actual position of the step-like intensity increase of the simulated signal. In contrast, 'false positive' values are those with $\theta_i > \gamma$ positioned not at the step. For a fixed window width 2w (figure 3.10), the detection

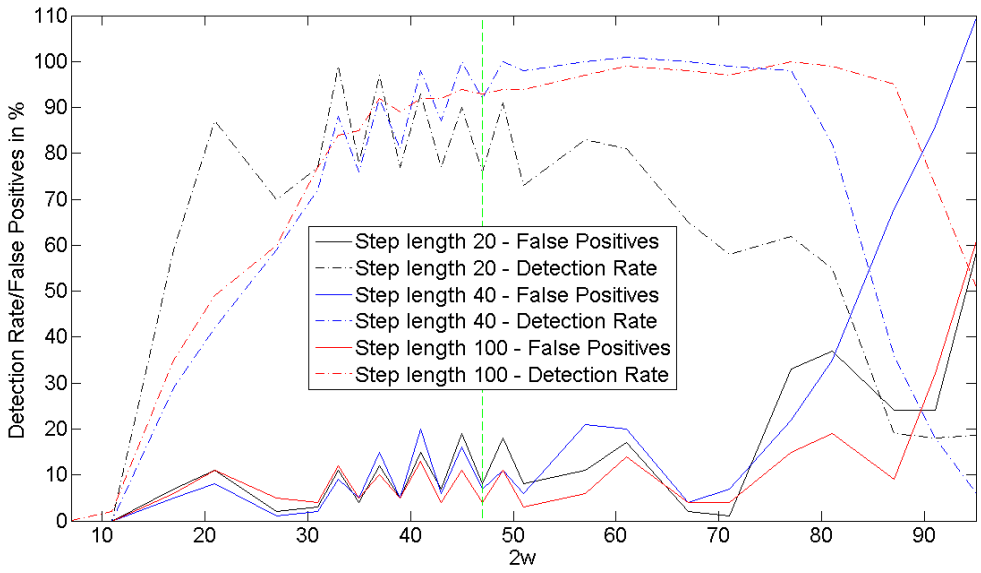

Figure 3.11: The detection rate and the percentage of detected false positives as a function of the width of the window, 2w. $\sigma = 1.6$, $\gamma = 100$

rate decreases for increasing σ, the width of the smoothing Gaussian kernel. This is reasonable since the smoother the data the more the steps will be washed out. A value of σ was chosen for which the detection rate is higher than 75% while no more than 10% of false positives are detected as indicated by the green line in figure 3.10. When σ is fixed (figure 3.11), the detection rate for the three different step lengths remains roughly constant between $35 < 2w < 55$ and then decreases rapidly. The percentage of false positives increases outside that same range of $35 < 2w < 55$. Thus, the choice of a 2w value in this parameter range is suitable to apply to the real data. The green dashed line in figure 3.11 marks the chosen value of 2w (48). Thus, for all subsequent

step detection these three parameters were chosen:

$$\sigma = 1.6, 2w = 48, \gamma = 100, \tag{3.8}$$

It is noteworthy that for such a small signal-to-noise ratio (SNR) of ~ 1.0 (SNR is defined as the step height divided by half the noise amplitude) used for the simulated data, the algorithm in [37] produced detection rates lower than 65%, whereas in my algorithm the detection rate stays above 75% even for step lengths of 20 frames and is above 90% for step lengths larger than 40 frames. The false positives are below 10% in all areas. While one reason for this discrepancy may lie in the fact that a slightly different simulated data set is used to obtain the optimal parameters of the step detection algorithm in [37], I also corrected their original equations to obtain m_i, t_i^l and t_i^r (equations 3.3, 3.4 and 3.5).

3.4.2 The rate of non-specific attachment

To estimate the rate of non-specific attachment of AMPPNP to the casein-coated surface, fifty 14x10 pixel areas were randomly chosen in a 230x200 pixel area surrounding the position of the lipid droplet in 249 video segments each of 60 s duration. The number of the randomly chosen 14x10 pixel areas guarantees that on average 15% of the area of 230x200 pixels surrounding the lipid droplet position is sampled. In the analysed 14x10 pixel areas, 2366 fluorescent spots were detected by the step detection algorithm. To compare this value with the rate of fluorescent events colocalizing with at the lipid droplets, the number of fluorescent spots has to be scaled by the 13x5 pixel region in which a fluorescent event occurs at the lipid droplet (see section 3.3).

Thus, the probability of a fluorophore appearing by non-specific attachment in an area

equal to the area associated with a lipid droplet (see figure 3.5) can be calculated as follows:

$$\frac{2366 \text{ events}}{50 \text{ areas probed}} \cdot \frac{5.8 \text{ video segments/lipid droplet}}{249 \text{ video segments}} \cdot \frac{13\text{x}5 \text{ pixel}}{14\text{x}10 \text{ pixel}} =$$

$$= 0.51 \ \frac{\text{events}}{\text{lipid droplet}} = 51\%$$

This is comparable to the 38% of lipid droplets colocalizing with an AMPPNP molecule (see section 3.3). Thus, it is very likely that most of the fluorophores that were found in the vicinity of the lipid droplets attached there non-specifically. A formal possibility exists that fluorescently labelled AMPPNP is not able to bind at the catalytic site of the motor head. However, this is highly unlikely because similar modifications of ATP still allow its binding to the motor's catalytic site [19].

Chapter 4

Conclusions and Outlook

A setup was built accompanied by the development of a detection methodology that allows studying motor regulation, *in-vitro*, by a fluorescently-labelled co-factor. This setup has the sensitivity and versatility to image the docking of a single co-factor to the motor complex while imaging the cargo position in pseudo DIC. A proof-of-principle experiment was performed where the regulator binds statically to the microtubule-tethered motor head with lipid droplets purified from *Drosophila* embryos being the examined motor-cargo complex, and fluorescently labelled AMPPNP being the regulator. However, a limitation of this experiment is the non-specific binding of the fluorophores to the surface, which limited the possibility of distinguishing specific binding of the regulator to the motors. Future experiments will have to be performed to test whether this limitation still holds when specific interaction is known to happen; for example by using active single motors attached to plastic beads. However, this experiment could not be realized currently due to the lack of purified kinesin but should be straight forward to be implemented in the future with the methodology I developed. Furthermore, future experiments where the regulator binds to the moving motor-cargo complex can quite easily be distinguished from non-specific attachment to the surface since the fluorophore will start moving with the motor-cargo complex.

Nevertheless, the non-specific attachment needs to be reduced for easier identification of

positive events in future experiments. Casein, used in the current work, is a commonly used blocking protein [11, 55] to study motor function *in-vitro*. However, casein aggregates into complexes that allow the kinesin tail to bind to the glass surface [38]. Hence, it is possible that other small molecules, as for example a fluorescently tagged regulator, may also bind between aggregates of adsorbed casein promoting non-specific surface attachment. Apart from coating the surface with casein, bovine serum albumin (BSA) is another commonly used blocking protein which reduces non-specific binding of motors [43] and fluorophores like quantum dots [34]. However, BSA, similar to casein, is a very large protein which does not result in optimal coverage of the surface. Thus, with a BSA coated surface, one may encounter a comparable non-specific binding rate of small molecules as is for casein. Another possibility is coating the surface with polyethlyene glycol (PEG). Previous work showed that non-specific adsorption of a protein (Rep protein) could be immensely reduced with PEG compared to a BSA surface coating [23]. However, protocols need to be developed to immobilize the microtubules on such surfaces as well as test non-specific binding of small molecules such as AMPPNP.

Another method to reduce non-specific attachment may be altering the initial AMPPNP concentration. The initial concentration of AMPPNP had to be chosen in the nM-range to avoid background fluorescence. At higher AMPPNP concentrations, no single fluorescent spots could be observed on the surface because of the bright background. A further decrease of the AMPPNP concentration would result in an increase of the time for a fluorescent event to occur which can be larger than the time the motor-cargo complex is attached to the microtubule. Additionally, a decrease of the initial AMPPNP concentration would not change the relative rates of specific versus non-specific attachment

because both rates will drop linearly with the initial concentration (see Appendix C).

For future experiments, the setup can be modified by mounting the far-red LED (used in [12]) in addition to the orange LED to allow switching between the two LEDs within the order of a few seconds. The orange LED can be used for visualizing microtubules during the time in which the motor-cargo complex is brought on top of one microtubule using the optical trap. Afterwards, the DIC light can be switched from the orange to the far-red LED. With the far-red LED, the motor-cargo complex is still visible in pseudo DIC. Furthermore, since the wavelength range of the far-red LED and of the fluorescence emission do not coincide, the position of the motor-cargo complex and of the fluorophore emission can be displayed simultaneously in two cameras as demonstrated previously [12]. This allows improving the quality of the acquired image sequences since exposure time and EM gain can be individually adjusted for each camera. A time-sharing cycle would not be necessary.

Another option for future experiments is to implement an additional TIRF excitation laser to image microtubules in fluorescence rather than in DIC. The position of fluorescently labelled microtubules can be estimated more precisely in TIRF microscopy than with DIC microscopy. However, the wavelength range of the fluorescently-labelled microtubules must not coincide with the emission spectrum of the fluorescently-labelled regulator which would require a different setup of filters and dichroic mirrors.

Appendices

Appendix A

Purification protocols

A.1 Microtubule preparation protocol

Preparation time: $\sim$ 60 min

Ingredients

- 5x PM (500 mM PIPES, 5 mM $MgSO_4$, 10 mM EGTA; stored at -80°C)
- Taxol (10 mM, diluted in DMSO; stored at -80°C)
- GTP (10mM, stored at -80°C)
- DB (35 mM PIPES, 5 mM $MgSO_4$, 1 mM EGTA, 0.5 mM EDTA; stored at -80°C)
- one pellet of kinesin tubulin (stored at -80°C)

Procedure

1. Warm up tubulin pellet (in tube) in hands until it is melted
2. Spin in centrifuge for 30 min at 6000 rpm
3. Dilute Taxol to 4 mM with DMSO

4. Prepare MTGB: 3.8 μl 5xPM, 5.7 μl ddH_2O, 3.8 μl 5xPM, 0.5 μl Taxol (4 mM), mix solution, then add 10μl GTP

5. After centrifugation, make 'concentrated MT': mix 35 μl of tubulin supernatant with 10 μl MTGB slowly with cut pipette tip

6. Incubate 'concentrated MT' in 37°C water bath for 20 min

7. Prepare DBMT (for 8-12 assays): 162 μl DB, 0.9 μl Taxol (4 mM), mix solution and add 18 μl GTP

8. Take 'concentrated MT' from water bath, mix slowly with cut pipette tip

9. Make 'MT': Add 2.7 μl 'concentrated MT' to DBMT

10. Mix all MT tubes slowly with cut pipette tip (MT last $\sim$ 12 days at 25°C)

A.2 Lipid droplet purification

Preparation time: $\sim$ 60 min

Ingredients

- MEPS 62.5 mM (K_2-PIPES 62.5 mM, EGTA 5 mM, $MgCl_2$ 5 mM, pH 7.2; stored at 4°C)
- DTT (100 mM; stored at -80°C)
- 2xPI (Dissolve one tablet of complete Mini EDTA-free from Roche in 0.75 ml ddH_2O; stored at -20°C)
- Pepstatin A (1 mM; stored at -20°C)
- PMSF (150 mM diluted in ETOH; stored at 4°C)
- Embryos of *Drosophila melanogaster* at $\sim$ 3h

Procedure

1. Remove agar plates from fly cups and replace it with a fresh agar plate with yeast
2. Carefully remove garbage from agar plates with wet brush
3. Bring embryos from agar plates in mesh tube by squirting ddH_2O on plates, swirling with brush and flushing them in the mesh tube with ddH_2O
4. Add 50%/50% v/v bleach/water solution, leave for 2:30 min, swirl every other 30 s for 30 s to dechorionate embryos.

5. Rinse with ddH_2O thoroughly

6. Scrap dechorinated embryos from mesh in a tube with razor blade

7. Add to tube with embryos: 170 μl MEPS, 18 μl DTT, 50 μl 2xPI, 1 μl Pepstatin A, 10 μl PMSF)

8. Gently mix with a Teflon-pestle to make a homogeneous solution

9. Centrifuge for 10 min at 10,000 rpm at 4°C

10. Extract white supernatant (enriched with lipid droplets) with a cold glass pipette

11. Make 'LD': Add 18 μl DTT and 50 μl 2xPI to supernatant

12. Keep LD on ice and immediately use it for lipid droplet assay

Appendix B

Sample Preparation

B.1 Preparation of lipid droplet assay

Ingredients

- MEPS 62.5 mM (K_2-PIPES 62.5 mM, EGTA 5 mM, $MgCl_2$ 5 mM, pH 7.2; stored at 4°C)
- Taxol (10 mM, diluted in DMSO; stored at -80°C)
- GTP (10mM; stored at -80°C)
- CDB (5.55 $\frac{\text{mg}}{\text{ml}}$ casein in DB; stored at -80°C)
- Glucose (2.5 M in ddH_2O; stored at 4°C)
- Glucooxidase (stored at -80°C)
- Catalase (stored at 4°C)
- MT (stored at 25°C)
- LD (kept on ice)
- EDA-AMPPNP labelled with TAMRA (Jena Bioscience, Cat No. NU-810-TAM, 1 mM, stored at -20°C)

Procedure

1. Prepare flow cell: Attach a coverslip coated with 0.02% Poly-L-lysine to a glass slide with a spacer (flow cell volume $\sim$ 10 μl)

2. Flush flow cell with 25-30 μl MT (see Appendix A1) and incubate for $\geq$ 20 min

3. Dilute Taxol to 4 mM with DMSO

4. Flush flow cells with 25-30 μl 'buffer': 162 μl MEPS, 0.9 μl Taxol, mix solution and add 18 μl GTP

5. Flush flow cell with 25-30 μl 5 mg/ml casein in blocking buffer (35mM PIPES, 5mM Mg_2SO_4, 1mM EGTA, 0.5mM EDTA, pH 7.2) to block the surfaces and incubte for $\geq$ 20 min

6. Dilute 0.5 μl AMPPNP to 100 nM with MEPS (this step is required only once a week; 100 nM AMPPNP diluted in MEPS can be kept at 4°C for up to 7 days)

7. Mix 'lipid droplet solution' (make it fresh for each sample): 80 μl MEPS, 5 μl DTT, 15 μl LD, 0.5 μl Taxol together with an oxygen-scavenging system of 50 U/ml glucose oxidase, 500 U/ml catalase and 12.5 mM glucose

8. Mix 9.5 μl lipid droplet solution with 0.5 μl AMPPNP (100 nM) for 5 nM AMPPNP

9. Flush in flow cell and immediately use sample

Appendix C

Model for diffusion of particles inside a box

A model was developed to estimate the dependence of the initial AMPPNP concentration c_0 with the attachment rate of AMPPNP on the surface and on the arrival time of an AMPPNP molecule to a specific spot on the surface like the motor head.

A cuboid with lengths x_0, y_0 and z_0 was used to model the flow cell. We assume that the surface blocking solution sticks to the bottom and top plane, but not the sides of the flow cell. This implies on our model that the particles can be adsorbed by the bottom and top plane of the box. The diffusion equation to solve is

$$\sum_{i=1}^{3} \frac{\partial^2 c}{\partial x_i^2} = \frac{1}{D}\frac{\partial c}{\partial t} \text{ with c} = \text{c}(\vec{x};\text{t}) \tag{C.1}$$

where D is the diffusion constant, x_i the position and t the time. Initially, the particles are randomly distributed in the cuboid ($\text{c}(\vec{x};\text{t=0}) = c_0$). The appropriate boundary conditions for this problem are [5]

$$\begin{aligned} \frac{\partial c}{\partial x}(x=0,y,z;t) &= 0 & \qquad \frac{\partial c}{\partial x}(x=x_0,y,z;t) &= 0 \\ \frac{\partial c}{\partial y}(x,y=0,z;t) &= 0 & \qquad \frac{\partial c}{\partial y}(x,y=y_0,z;t) &= 0 \\ c(x,y,z=0;t) &= 0 & \qquad c(x,y,z=z_0;t) &= 0 \end{aligned}$$

The concentration is then calculated by

$$c(\vec{x};t) = c_0 \int_0^{x_0} \int_0^{y_0} \int_0^{z_0} dx'dy'dz' \mathrm{v}(\vec{x},\vec{x'};t) \tag{C.2}$$

where v($\vec{x}$,$\vec{x'}$;t) is the Green's function of the 3D diffusion equation which can be composed out of the 1D Green's functions since the boundary conditions can be separated. The solution for the Green's function is [15]

$$v(\vec{x},\vec{x'};t) = \frac{1}{x_0}\left(1 + 2\sum_{l=1}^{\infty} exp\left(-Dt\left(\frac{l\pi}{x_0}\right)^2 t\right) cos\left(\frac{l\pi x}{x_0}\right) cos\left(\frac{l\pi x'}{x_0}\right)\right) \tag{C.3}$$

$$\cdot \frac{1}{y_0}\left(1 + 2\sum_{m=1}^{\infty} exp\left(-Dt\left(\frac{m\pi}{y_0}\right)^2 t\right) cos\left(\frac{m\pi y}{y_0}\right) cos\left(\frac{m\pi y'}{y_0}\right)\right) \tag{C.4}$$

$$\cdot \frac{2}{z_0}\left(\sum_{n=1}^{\infty} exp\left(-Dt\left(\frac{n\pi}{z_0}\right)^2 t\right) sin\left(\frac{n\pi z}{z_0}\right) sin\left(\frac{n\pi z'}{z_0}\right)\right) \tag{C.5}$$

The number of particles P(t) which at time t remained in the diffusion space is calculted by

$$P(t) = \int_V dV c(\vec{x};t) = c_0 \int_0^{x_0} \int_0^{y_0} \int_0^{z_0} dxdydz \int_0^{x_0} \int_0^{y_0} \int_0^{z_0} dx'dy'dz' v(\vec{x},\vec{x'};t) \tag{C.6}$$

which leads to

$$P(t) = c_0 \sum_{n=1}^{\infty} \frac{2}{\pi^2} x_0 y_0 z_0 \frac{1}{n^2} \left(cos(n\pi) - 1\right)^2 exp\left(-Dt\left(\frac{n\pi}{z_0}\right)^2 t\right) \tag{C.7}$$

Thus the number of particles left in the solution after time t is proportional to the initial particle concentration c_0.

Appendix D

Component List

Important components of the microscope are shown in the table below based on figure 2.6. The setup of the optical trap remained unchanged and is illustrated in [12].

Part	Manufacturer	Part Number
Light Sources		
TIRF (532 nm)	Chrystalaser	CL532-100-O
Trap (830 nm)	Omicron Laser	LDM830.200.CWA.L
LED	Thorlabs	M590L2-C3
EMCCD	Andor	iXon+ 897
Dichroics and Filters		
DM	Semrock	FF750-SDi02
Turret 1 'diagonal'	Semrock	Di01R532
Turret 1 'bottom'	Semrock	BLP01-532R-25
Turret 1 'left'	Chroma	NC279278 - ZET532/10x
Turret 2 'diagonal'	Semrock	FF750-SDi02
Turret 2 'bottom'	Semrock	SP01-785RU-25
Filter cube 'diagonal'	Semrock	FF670-SDi01
Filter cube 'bottom'	Semrock	BLP01-635R
Filter cube 'right'	Semrock	FF-1-607/70

Bibliography

[1] http://www.crystalaser.com , consulted 09/11/2013.

[2] http://www.lifetechnologies.com, consulted 06/09/2013.

[3] http://micro.magnet.fsu.edu/primer/techniques/dic/dicintro.html, consulted 12/3/2013.

[4] http://www.thorlabs.com, consulted 03/25/2013.

[5] G. Adam and Delbrück M. Reduction of Dimensionality in Biological Diffusion Processes. In A. Rich and N. Davidson, editors, *Structural Chemistry and Molecular Biology*. 1968.

[6] S. Ally, A.G. Larson, K. Barlan, S.E. Rice, and V.I. Gelfand. Opposite-polarity motors activate one another to trigger cargo transport in live cells. *J Cell Biol*, 187, 2009.

[7] E.J. Ambrose. A Surface Contact Microscope for the study of Cell Movements. *Nature*, 1956.

[8] E.K. Anderson and D.S. Martin. A fluorescent GTP analog as a specific, high-precision label of microtubules. *Biotechniques*, 2011.

[9] A. Ashkin. Acceleration and Trapping of Particles by Radiation Pressure. *Phys. Rev. Lett.*, 24, 1970.

[10] D. Axelrod. Cell-substrate contacts illuminated by total internal reflection fluorescence. *The Journal of Cell Biology*, 1981.

[11] T.F. Bartsch, R.A. Longoria, E.-L. Florin, and G.T. Shubeita. Lipid Droplets Purified from Drosophila Embryos as an Endogenous Handle for Precise Motor Transport Measurements. *Biophysical Journal*, 105, 2013.

[12] A. Bayerle. Coincident time-shared single molecule imaging, manipulation and bright-field microscopy. Master's thesis, University of Texas at Austin, 2011.

[13] F. Bestvater, E. Spiess, G. Stobrawa, M. Hacker, T. Feurer, T. Porwol, U. Berchner-Pfannschmidt, C. Wotzlaw, and H. Acker. Two-photon fluorescence absorption and emission spectra of dyes relevant for cell imaging. *Journal of Microscopy*, 208, 2002.

[14] J.B. Bingham, S.J. King, and T.A. Schroer. Purification of dynactin and dynein from brain tissue. *Methods in enzymology*, 298, 1998.

[15] H.S. Carslaw and J.C. Jaeger. *Conduction of Heat in Solids, Second Edition*. Oxford University Press, 1959.

[16] B. C. Carter, G. T. Shubeita, and S. P. Gross. Tracking Single Particles: a User-Friendly Quantitative Evaluation. *Physical Biology*, 2, 2005.

[17] D.J. Denvir and C.G. Coates. Electron-multiplying CCD technology: application to ultrasensitive detection of biomolecules. *Proceeding of SPIE 4626*, 2002.

[18] N. D. Derr, B. S. Goodman, R. Jungmann, A. E. Leschziner, W. M. Shih, and S. L. Reck-Peterson. Tug-of-War in Motor Protein Ensembles Revealed with a Programmable DNA Origami Scaffold. *Science*, 338, 2012.

[19] T. Funatsu, Y. Harada, H. Higuchi, M. Tokunaga, K. Saito, Y. Ishii, RD. Vale, and T. Yanagida. Imaging and nano-manipulation of single biomolecules. *Biophys Chem.*, 68, 1997.

[20] S.P. Gross, M.A. Welte, S.M. Block, and E.F. Wieschaus. Dynein-mediated cargo transport in vivo. A switch controls travel distance. *J Cell Biol*, 148, 2000.

[21] S.P. Gross, M.A. Welte, S.M. Block, and E.F. Wieschaus. Coordination of opposite-polarity microtubule motors. *J Cell Biol*, 156, 2002.

[22] B. Gutiérrez-Medina and S.M. Block. Visualizing individual microtubules using bright-field microscopy. *American Journal of Physics*, 78, 2010.

[23] T. Ha, I. Rasnik, W. Cheng, H.P. Babcock, G.H. Gauss, T.M. Lohman, and S. Chu. Initiation and re-initiation of DNA unwinding by the Escherichia coli Rep helicase. *Nature*, 419, 2002.

[24] A.G. Hendricks, E. Perlson, J.L. Ross, H.W. Schroeder, M. Tokito, and E.L. Holzbaur. Motor coordination via a tug-of-war mechanism drives bidirectional vesicle transport. *Curr Biol.*, 20, 2010.

[25] E.L.F. Holzbaur and Y.E. Goldman. Coordination of Molecular Motors: From in vitro Assays to Intracellular Dynamics. *Curr Opin Cell Biol.*, 22, 2010.

[26] A. Ishijima, H. Kojima, T. Funatsu, M. Tokunaga, H. Higuchi, H. Tanaka, and T. Yanagida. Simultaneous observation of individual ATPase and mechanical events by a single myosin molecule during interaction with actin. *Cell*, 92, 1998.

[27] C. Leidel, R.A. Longoria, F.M. Gutierrez, and Shubeita G.T. Measuring Molecular Motor Forces In Vivo: Implications for Tug-of-War Models of Bidirectional Transport. *Biophysical Journal*, 103, 2012.

[28] A. Lesslett. Principles and Applications of Differential Interference Contrast Light Microscopy. *Microscopy and Analysis Light Microscopy Supplement*, 2006.

[29] R. Mallik and S.P. Gross. Molecular Motors: Strategies to Get Along. *Current Biology,*, 14, 2004.

[30] A.D. Mehta, Ronald S. Rock, Matthias Rief, James A. Spudich, Mark S. Mooseker, and Richard E. Cheney. Myosin-V is a processive actin-based motor. *Nature*, 400, 1999.

[31] M.T. Mesngon, C. Tarricone, S. Hebbar, A.M. Guillotte, E.W. Schmitt, L. Lanier, A. Musacchio, S.J. King, and D.S. Smith. Regulation of Cytoplasmic Dynein ATPase by Lis1. *The Journal of Neuroscience*, 26, 2006.

[32] S. Millecamps and J.-P. Julien. Axonal transport deficits and neurodegenerative diseases. *Nature Reviews Neuroscience*, 14, 2013.

[33] M. J. I. Mueller, S. Klumpp, and R. Lipowsky. Tug-of-war as a cooperative mechanism for bidirectional cargo transport by molecular motors. *Proc. Natl. Acad. Sci. USA*, 105, 2008.

[34] S.R. Nelson, M. Yusuf Ali, and D.M. Warshaw. Quantum Dot Labeling Strategies to Characterize Single-Molecular Motors. *Methods Molecular Biology*, 778, 2011.

[35] K. Neuman, E.H. Chadd, G.F. Liou, K. Bergman, and S.M. Block. Characterization of photodamage to Escherichia coli in optical traps. *Biophys. J.*, 77, 1999.

[36] K.C. Neuman and S.M. Block. Optical trapping. *Review of Scientific Instruments*, 75, 2004.

[37] J. Opfer and K.-E. Gottschalk. Identifying Discrete States of a Biological System Using a Novel Step Detection Algorithm. *PLoS ONE*, 7, 2012.

[38] T. Ozeki, V. Verma, M. Uppalapati, Y. Suzuki, M. Nakamura, JM. Catchmark, and WO. Hancock. Surface-Bound Casein Modulates the Adsorption and Activity of Kinesin on SiO_2 Surfaces. *Biophysical Journal*, 96, 2009.

[39] T. Perkins. Optical traps for single molecule biophysics: a primer. *Laser and Photonics Reviews*, 3, 2009.

[40] E. Perlson, S. Maday, MM. Fu, AJ. Moughamian, and EL. Holzbaur. Retrograde axonal transport: pathways to cell death? *Trends in Neurosciences*, 2010.

[41] AK. Rai, A. Rai, AJ. Ramaiya, R. Jha, and R. Mallik. Molecular Adaptations Allow Dynein to Generate Large Collective Forces inside Cells. *Cell*, 152, 2013.

[42] I. Rasnik, S. Myong, W. Cheng, T.M. Lohman, and T. Ha. DNA-binding Orientation and Domain Conformation of the E. coli Rep Helicase Monomer Bound to a Partial Duplex Junction: Single-molecule Studies of Fluorescently Labeled Enzymes. *Journal of Molecular Biology*, 336, 2004.

[43] S.L. Reck-Peterson, N.D. Derr, and N. Stuurman. Imaging Single Molecules Using Total Internal Reflection Fluorescence Microscopy (TIRFM). *Cold Spring Harb Protoc*, 2010, 2010.

[44] LT. Reiter, L. Potocki, S. Chien, M. Gribskov, and E. Bier. A Systematic Analysis of Human Disease-Associated Gene Sequences In Drosophila melanogaster. *Genome Research*, 11, 2001.

[45] S.T. Ross, S. Schwartz, J.T. Fellers, and M.W. Davidson. Total Internal Reflection Fluorescence (TIRF) Microscopy. Retrieved 01/19/2013.

[46] M.J. Schnitzer and Steven M. Block. Kinesin hydrolyses one ATP per 8-nm step. *Nature*, 388, 1997.

[47] P.R. Selvin and T. Ha. *Single-Molecule Techniques: A Laboratory Manual*. Cold Spring Harbor Laboratory Press, 2008.

[48] G.T. Shubeita, S.L. Tran, J. Xu, M. Vershinin, S. Cermelli, S.L. Cotton, M.A. Welte, and S.P. Gross. Consequences of motor copy number on the intracellular transport of kinesin-1-driven lipid droplets. *Cell*, 135, 2008.

[49] V. Soppina, A.K. Rai, A.J. Ramaiya, P. Barak, and R. Mallik. Tug-of-war between dissimilar teams of microtubule motors regulates transport and fission of endosomes. *PNAS Early Edition*, 2009.

[50] K.R. Spring and M.W. Davidson. Introduction to Fluorescence Microscopy. Retrieved 01/19/2013.

[51] M.C. Tuma and V.I. Gelfand. Molecular mechanisms of pigment transport in melanophores. *Pigment Cell Research*, 12, 1999.

[52] S. Uemura, K. Kawaguchi, J. Yajima, M. Edamatsu, Y. Toyoshima, and S. Ishiwata. Kinesin–microtubule binding depends on both nucleotide state and loading direction. *PNAS*, 99, 2002.

[53] R.D. Vale. The molecular motor toolbox for intracellular transport. *Cell*, 112, 2003.

[54] M.A. van Dijk, L.C. Kapitein, J. van Mameren, C.F. Schmidt, and E.J.G. Peterman. Combining optical trapping and single-molecule fluorescence spectroscopy: enhanced photobleaching of fluorophores. *J Phys Chem B*, 2004.

[55] M. Vershinin, B.C. Carter, D.S. Razafsky, S.J. King, and S.P. Gross. Multiple-motor based transport and its regulation by Tau. *PNAS*, 104, 2007.

[56] M.-L. Visnapuu, D. Duzdevich, and E.C. Greene. The importance of surfaces in single-molecule bioscience. *Molecular BioSystems*, 4, 2008.

[57] Y. Vugmeyster, E. Berliner, and J. Gelles. Release of Isolated Single Kinesin Molecules from Microtubules. *Biochemistry*, 37, 1998.

[58] C. Weaver, C. Leidel, L. Szpankowsk, NM. Farley, GT. Shubeita, and LS. Goldstein. Endogenous GSK-3/shaggy regulates bidirectional axonal transport of the amyloid precursor protein. *Traffic*, 14, 2013.

[59] M.A. Welte. Bidirectional transport along microtubules. *Current Biology*, 14, 2004.